

UNIVERSITY OF CAMBRIDGE

PART III PROJECT

DEPARTMENT OF PHYSICS

Interfacial tensiometry using checkerboard decomposition, a sharp tilting edge, and a 3D printed trough

Author:
BGN: 8266X

Supervisor:
Prof. Pietro Cicuta

May 16, 2022

Interfacial tensiometry using checkerboard decomposition, a sharp tilting edge, and a 3D printed trough

BGN: 8266X

May 16, 2022

Abstract

In this project, I designed, built, and tested a device for measuring capillary lengths using an imaging technique known as fast checkerboard decomposition. The main device consisted of a motor and rotary encoder used to control the tilt of a razor blade. This blade was used to deform the surface of water contained in a 3D printed trough. Refraction at the air-water interface caused distortions of a checkerboard pattern displayed below the trough. Using an overhead camera, images of this deformation could be taken. To display the checkerboard, I introduce a novel idea of using an inexpensive LCD which proved to be advantageous over the more conventional method of printing the checkerboard. Fast checkerboard decomposition was then used to find the gradient of the surface and reconstruct the interface shape. By fitting analytical solutions to this surface the capillary length was extracted. Using the motor, surfaces for different tilt angles could be collected and analysed. This showed that even at small angles the difference between the first-order exponential solution and the measured interface was detectable. Systematic differences likely caused by the initial filling of the trough was found to limit the precision of the device, despite this, the capillary length of water was measured as $2.69 \pm 0.05\text{mm}$ which is in good agreement with literature values.

Contents	Appendices	15
1 Introduction	Appendix A A solution to the Young-Laplace equation for a straight edge	15
1.1 Motivation	2	
1.2 Previous research	2	
1.2.1 Conventional techniques	2	
1.2.2 Moleai & Crocker's device	2	
1.2.3 Previous work with FCD	2	
1.3 Aims of the project	4	
2 Theoretical background	Appendix B Data acquisition & methodology	16
2.1 The shape of the fluid interface	4	
2.2 Fast checkerboard decomposition	4	
2.2.1 Displacement due to refraction	4	
2.2.2 Obtaining the displacement field	6	
3 Implementation	Appendix C Pinning & hysteresis	17
3.1 Design	4	
3.2 Scale calibration	6	
4 Results and discussion	Appendix D Determination of fill volume from Fourier domain	18
4.1 Fitting data to theoretical predictions	4	
4.2 Precision of the device	9	
5 Conclusions	Supporting tests and data	21
6 Further work	S.1 Tests of the device	21
	S.1.1 Negative tilt angles	21
	S.1.2 Checkerboard size	21
	S.1.3 Checkerboard translations	21
	S.1.4 Camera distance	23
	S.1.5 Capillary length over time	23
	S.1.6 Measuring a DPPC monolayer	24
	S.2 Testing a circular tilting interface	26
	S.2.1 Theoretical perspective	26
	S.2.2 Method and results	29
	12	
	12	

1 Introduction

1.1 Motivation

Surface tension is a measure of the energy required to form a unit of area between two fluids[1]. Measurement and understanding of surface tension is critical to many applications in industry and commercial products[2–4] including 3D printing[5]. Consequently, accurate measurement of this property is of vital importance. Many methods exist to measure surface tension including the Wilhelmy balance and the pendant drop. These methods have different advantages and limitations but often are expensive. For this reason, the idea behind this project is to build and test an inexpensive way to measure surface tension. A device recently proposed by Moleai & Crocker[6] will form the basis of this investigation. I present several improvements to their apparatus, including an LCD to perform fast checkerboard decomposition, an imaging technique I use to measure the fluid interface.

1.2 Previous research

1.2.1 Conventional techniques

Traditionally, surface tension has been measured by one of the devices depicted in Fig.1, although others exist. These typically employ highly symmetric geometry to control and then measure the surface. These methods generally fall into two categories depending on how the tension in the fluid surface is created: contact angle or gravity. In this project, I employ the latter. Gravity techniques measure the shape of the fluid interface generated by the balance of gravitational and interfacial forces. Then, by fitting to the shape of the interface, the surface tension is extracted. Gravity based techniques generally require the use of numerical methods[7] to fit the data to predicted profile shapes. Typically, these methods have an associated accuracy of 0.1 mN m^{-1} [8].

1.2.2 Moleai & Crocker's device

The device presented in this report takes its origin from the device presented by Moleai & Crocker[6]. Their paper presented a 3D printed device that used sharp disks co-planer to the fluid interface. These disks were then tilted along an axis also in this plane. This created a symmetric meniscus profile that was then imaged. A diagram of their device is shown in Fig.2. To image the meniscus, Moleai & Crocker illuminated the interface with a telecentric light source that passed through the side of the measurement apparatus. A photo of the silhouette created by the meniscus was then taken, this is shown in Fig.3. Edge detection algorithms were then used to find the meniscus in these images.

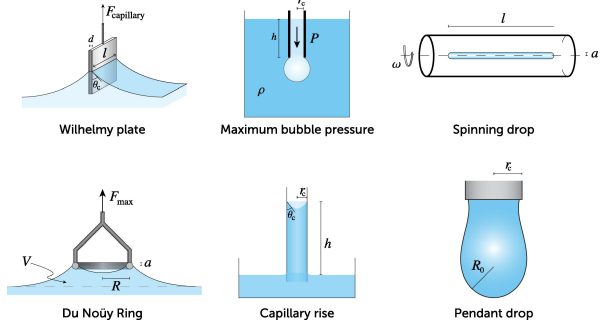


Figure 1: Diagrams of various methods currently used to measure the surface tensions of liquids. Adapted from Drellich et al.[10].

By comparing this edge to a library of numerically generated surfaces created by Surface Evolver[9]¹ the interfacial tension could be extracted.

Moleai & Crocker were able to accurately measure the surface tension of water but discovered that the sensitivity is limited by the Bond number, a measure of the relative importance of interfacial and gravitational forces[10, 11]. For this device, this was principally determined by the tilt angle, with larger Bond numbers corresponding to larger tilt angles. Smaller changes in surface tension were therefore detectable at larger tilt angles due to larger changes in the surface profile that were observed. Overall, they were able to achieve an accuracy of $\pm 0.1 \text{ mN m}^{-1}$ for water.

1.2.3 Previous work with FCD

The method of fast checkerboard decomposition (FCD) has been implemented before[12–18]. The method typically consists of a checkerboard or other known pattern being placed below an optically transparent interface as shown in Fig.4. By taking photographs, measurements of the displacement due to the refraction are made. From this, the surface profile can be extracted, this is discussed in Section 2.2.2. FCD is often compared to an alternative: digital image correlation (DIC), a method that has been developed to measure strain in a lattice[19]. Previous implementations of FCD have been used to measure simple situations as a proof of concept, for example, measuring the shape of a plano-concave lens of known geometry[13] or objects floating on the water's surface[12]. These investigations have extended to cover other aspects of the method such as occlusions[15]. Also discussed are the limitations on fluid height and checkerboard size so the displacement field can be recovered. These previous implementations have found a vertical precision of $<1 \mu\text{m}$ [12, 13]. This methodology has previously been successful in measuring water's surface tension by measuring capillary waves[14].

¹An open-source program for simulating fluid interfaces.

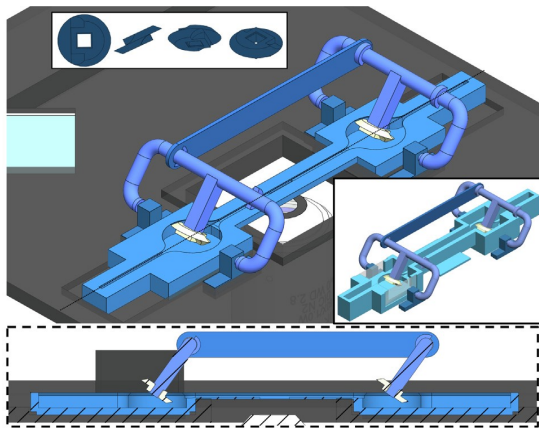


Figure 2: Diagram of the apparatus developed by Moleai & Crocker taken from their paper[6] showing two tilting disks in separate troughs connected by a linkage.

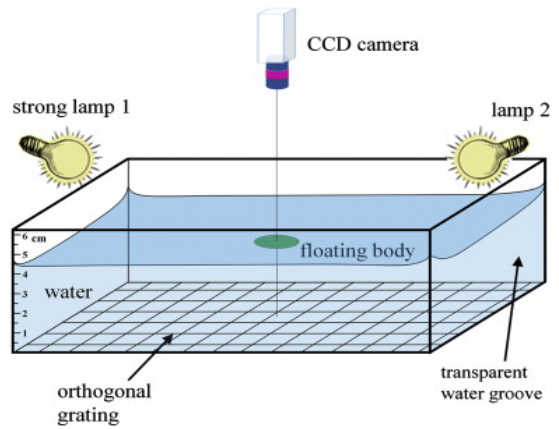


Figure 4: Diagram of the typical setup for FCD. Adapted from Liu et al.[12]

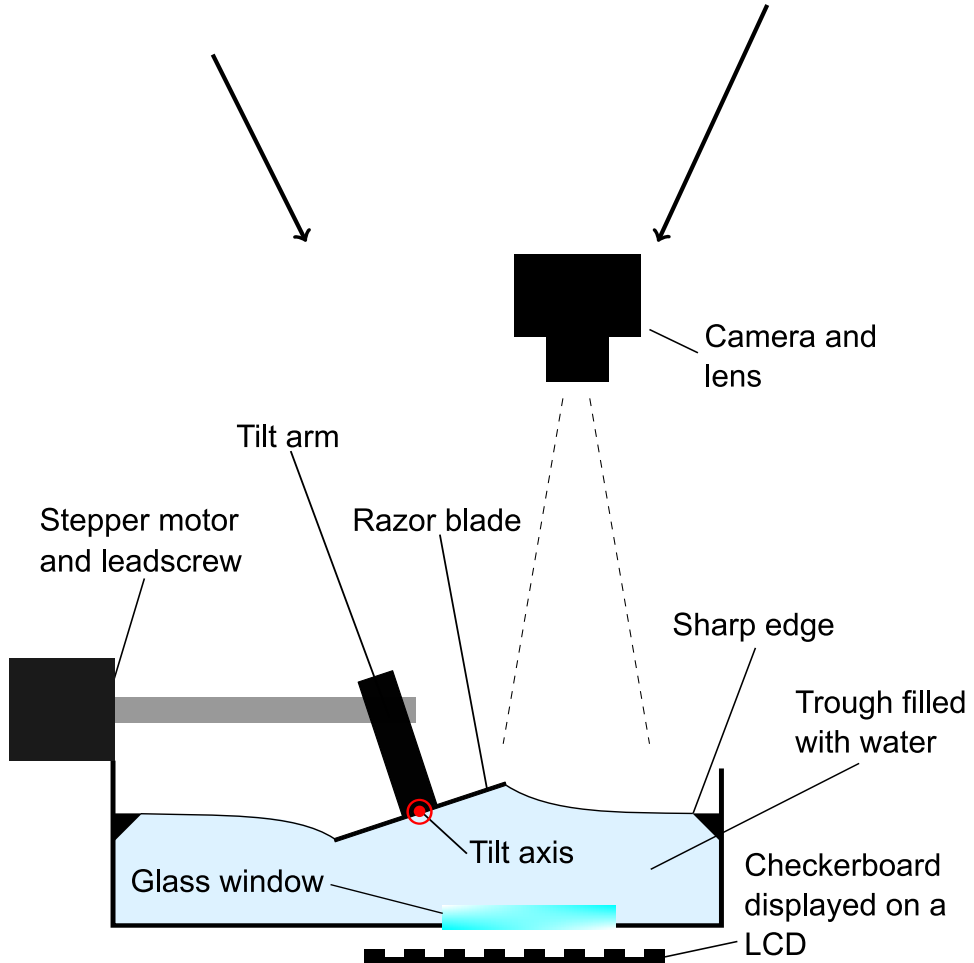


Figure 5: Cross-section of the final apparatus developed in this investigation. Elements from Fig.2 and Fig.4 have been combined and adapted to produce a new device. Also shown are new additions of a motor and LCD.

1.3 Aims of the project

I aim to design, build, and test a device similar to the one proposed by Moleai & Crocker. However, to avoid some of their alignment issues and to explore an alternative measurement procedure (FCD), I will closely follow the work of Wildeman[15] including using the algorithms developed. Unlike conventional FCD, I propose an alternative apparatus design, where a glass window in the otherwise 3D printed trough allows an LCD displaying the checkerboard to be observed from above, see Fig.5. I accompany this with several smaller changes to Moleai & Crocker's device, including using:

- A readily available razor blade as the tilting interface,
- Analytical solutions to model the interface,
- A motor and rotary encoder to change and measure the angle of the tilting interface,
- A fused deposition modelling printer, and
- A large square outer perimeter rather than a small concentric circle.

These changes and the overall implementation of the device are explained in Section 3. In this project, I focus on using analytical solutions for the shape of the interface. This is done to improve the accessibility of the device due to the significantly lower computational resources required over alternatives, such as those used by Moleai & Crocker. A discussion of these solutions is in Section 2.1. This is followed by the theory behind FCD in Section 2.2. To test the device, the capillary length, which is proportional to the square root of surface tension, was measured for pure water. Details of these results are contained in Section 4, with some additional tests analysed in the supplementary data. Some overall conclusions and areas in need of further study are discussed in Sections 5 and 6.

2 Theoretical background

2.1 The shape of the fluid interface

Here I follow a discussion similar to Bush[20] and Rusanov[21]. Who show for a static interface between two fluids, the balance of forces at an interface leads to the Laplace-Young equation given by

$$\Delta p = \gamma \nabla \cdot \mathbf{n}, \quad (1)$$

where Δp is the pressure difference between the two sides of the interface, γ is the surface tension and \mathbf{n} the surface normal. In a gravitational field, this pressure difference is predominantly from hydrostatic pressure and therefore $\Delta p = \Delta \rho g h$. $\Delta \rho$ is the density difference between the fluids.

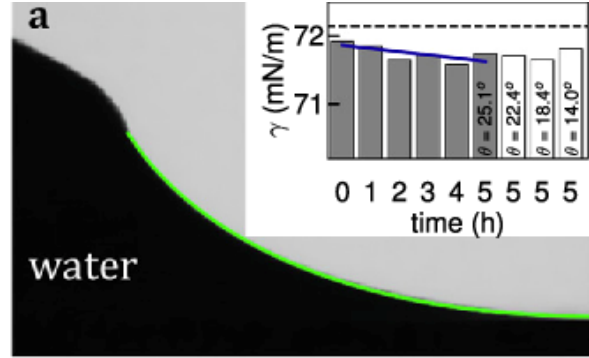


Figure 3: An example of the meniscus imaged by Moleai & Crocker[6]. Imaging from the side means only the profile of the ridge created by a disk could be measured. In my project imaging from above meant, other tilting geometries could be used.

For interfaces such as those discussed in this project, the analytic form of $\nabla \cdot \mathbf{n}$ can then be found in terms of the height of the surface, h , and in principle, Eq.(1) can be solved if the boundary conditions are known[21]. This is often difficult or impossible to do analytically and must in general be done numerically[7]. However, in this project, approximate solutions can be found. Modelling the fluid interface and razor blade as shown in Fig.6, this problem can be examined in one dimension and the Young-Laplace equation becomes[22]

$$\gamma \frac{h_{xx}}{(1 + h_x^2)^{3/2}} = \rho g h. \quad (2)$$

To first-order, the solution is

$$h(x) = w \sin(\alpha) \exp(-(x - w \cos(\alpha))/l_c), \quad (3)$$

as shown in Appendix A. With x measured from the tilt axis and $2w$ is the width of the razor. l_c is the capillary length of the fluid, equal to $\sqrt{\frac{\gamma}{\Delta \rho g}}$, and α is the angle the razor is tilted from horizontal. This is the solution that will be fitted to the surfaces generated by FCD.

2.2 Fast checkerboard decomposition

2.2.1 Displacement due to refraction

This measurement technique is based on the apparent displacement caused by refraction, hence governed by Snell's law

$$n_a \sin(\theta) = n_w \sin(\delta). \quad (4)$$

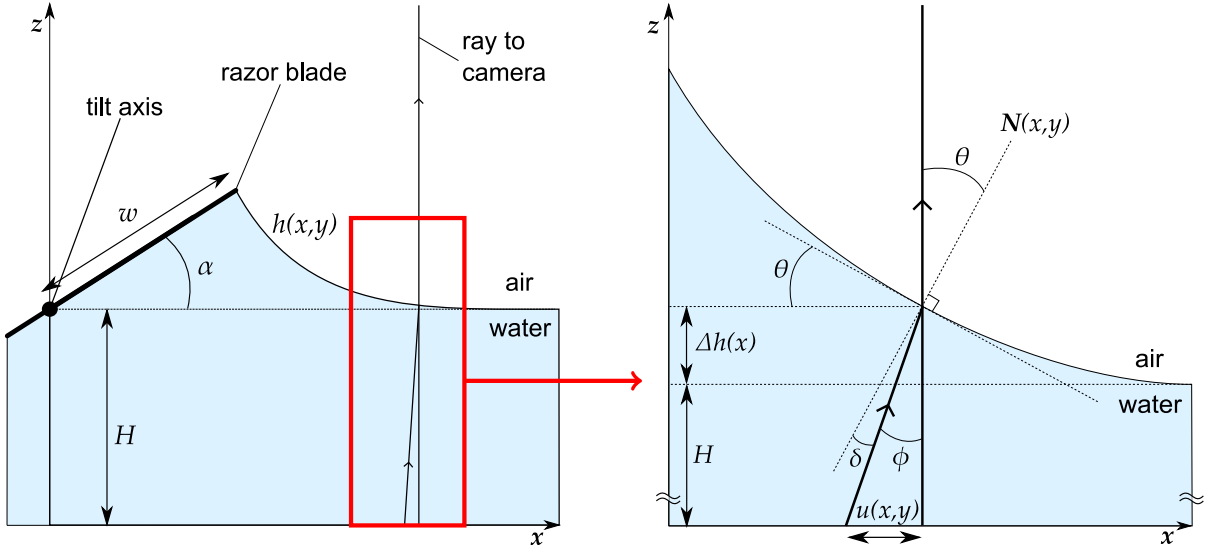


Figure 6: A cross-section diagram of the meniscus created by a razor blade of width $2w$ raised at an angle α . H is the undisturbed water depth. Also shown is a ray from below diffracted to the camera. This is shown in more detail in Fig.7.

From Fig.7, showing the geometry of the apparent displacement caused by refraction, we find $\phi = \theta - \delta$ and therefore

$$\frac{u(x,y)}{H + \Delta h(x,y)} = \tan(\phi) = \frac{\tan(\theta) - \tan(\delta)}{1 + \tan(\theta) \tan(\delta)}. \quad (5)$$

Combining with Snell's law and trigonometric formulae gives

$$\frac{u(x,y)}{H + \Delta h(x,y)} = \frac{\tan(\theta)(\sqrt{n^2 + (n^2 - 1)\tan(\theta)} - 1)}{\sqrt{n^2 + (n^2 - 1)\tan(\theta)} + \tan^2(\theta)}, \quad (6)$$

where $n = n_w/n_a$. To first-order this is

$$u(x,y) = (H + \Delta h)(1 - \frac{1}{n}) \tan(\theta). \quad (7)$$

Hence, for small θ and small overall height changes, such that

$$\Delta h_{max} = w \sin(\alpha) \ll H, \quad (8)$$

$u(x,y)$ is proportional to the gradient of the surface. So the heightmap, $h(x,y)$, can be found directly by integration of $u(x,y)$.

These approximations limit the scope of the experiment to small α . As shown in Appendix A this is also the region where the first-order solution to the Young-Laplace is valid.

Other implementations of FCD[12,13,18], show it is possible to obtain $h(x,y)$ without making these approximations at the cost of computation time. This is not explored here, instead, we note that

Figure 7: Schematic of the geometry of a ray from the LCD being diffracted to the camera above. This is used to derive the relation between displacement, $u(x,y)$, and the gradient of the surface, $\tan(\theta)$.

with these approximations both, Eq.(7) and Eq.(3) are proportional to overall constants dependent on the physical parameters. These constants can be ignored and instead replaced by a single overall vertical scaling parameter determined during the fitting procedure. This limits the ability to test the accuracy of the theoretical predictions for these constants but has the advantage that the geometric and optical parameters do not need to be measured. This is particularly useful for the refractive index which could in principle change with additions to the surface such as in Section S.1.6 or in general, might not be known. This methodology works only for first-order approximations which limits the scope of this approach.

I have presented this analysis in one dimension. A general surface gradient can be found by performing the same construction in an orthogonal direction using the displacement field $\mathbf{u}(\mathbf{r}) = u_x(x,y)\mathbf{i} + u_y(x,y)\mathbf{j}$

Moisy et al.[14] expand this analysis to a geometry where the measured displacement, $u(x,y)$, is not coplanar with the bottom of the tank but instead separated by a glass plane and air gap. This is the configuration adopted in this investigation. They show H becomes an effective depth equal to

$$H_{eff} = H + \frac{n_w}{n_g} h_g + \frac{n_w}{n_a} h_a, \quad (9)$$

with $n_{g/a}$ being the refractive index, and $h_{g/a}$ being the depth of the glass or air respectively. Therefore, this amounts to changing the value of H , so can be neglected in this investigation.

2.2.2 Obtaining the displacement field

To complete the system of equations the displacement field $\mathbf{u}(\mathbf{r})$ must be obtained. Below I outline the work of Shi et al.[13] and Wildeman[15] and who describe the FCD method. Wildeman[15] shows the image distorted by refraction is given by

$$\begin{aligned} I(\mathbf{r}) &= I_0(\mathbf{r} - \mathbf{u}(\mathbf{r})) \\ &= \sum_{m=-\infty}^{\infty} \sum_{n=-\infty}^{\infty} a_{mn} e^{i(m\mathbf{k}_1 + n\mathbf{k}_2) \cdot (\mathbf{r} - \mathbf{u}(\mathbf{r}))}. \end{aligned} \quad (10)$$

I_0 is an original reference image that is distorted by $\mathbf{u}(\mathbf{r})$. Writing this as a Fourier series we observe that the $\mathbf{u}(\mathbf{r})$ acts to modulate the phase of each term in the series. For small $\mathbf{u}(\mathbf{r})$ the effect of this is limited to the region around the carrier peaks. Filtering in the Fourier domain extracts the individual terms of this series. This requires the carrier peaks to be well defined. In this project, this is fulfilled using a checkerboard pattern. Nyquist's theorem would predict that a sinusoidal pattern would be ideal, however, this is not possible with the resolution of the LCD used. To locate the positions of these carrier peaks it is first necessary to take a reference image, I_0 , of the undisturbed surface ($\alpha = 0^\circ$). A comparison of a reference image and a corresponding distorted image is shown in Fig.8.

In the region around each carrier peak, the phase can be found by taking the complex logarithm. As Wildeman discusses[15] “doing this for two linearly independent reciprocal vectors” gives two equations which can then be solved to give $\mathbf{u}(\mathbf{r})$. Shi et al.[13] and Wildeman[15] highlight that conventional implementations of the complex logarithm return only the principal value, thus causing jumps of 2π . Correcting this was found to be imperative during this experiment.

3 Implementation

The final design of the apparatus is shown in Figs.9 and 10. The numbered annotations in these photographs correspond to the numbered paragraphs below. A discussion of how this apparatus was used to collect data is contained in Appendix B.

3.1 Design

1 LCD The FCD method requires a checkerboard to be imaged below the water surface. Lighting, particularly glare was found to affect the quality of the data. I propose an alternative solution to the conventional desk lamp, using an LCD. Lighting and the displaying checkerboard could be achieved by mounting the relatively inexpensive Hyperpixel[23] display to a Raspberry Pi[24]. The LCD illuminates the surface in a way that is uniform, reproducible,

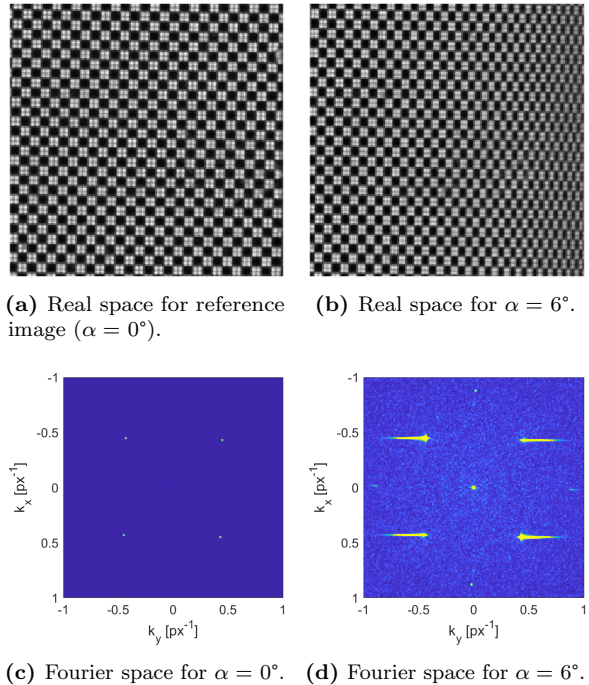


Figure 8: Comparison of the reference and distorted images. The real-space images are 200x200px extracts from 918x864px images used to generate Fig.14c. Also shown are extracts of the central region in Fourier space.

and does not create glare. There are several other advantages including the ability to easily change the checkerboard size, position, brightness, etc.

The displayed checkerboards were made by generating images with the same pixel width and height as the screen; individual pixels were coloured to create a checkerboard. These images were displayed in full so no interpolation or approximations were made by the screen. This method leads to sharp edges of each square although is limited by the resolution of the screen. Examples can be seen in Fig.11.

2 Window To observe the LCD, a precision glass window[25], made watertight using an O-ring and PTFE tape, was installed in the trough. Placing the checkerboard below the water with a glass window has the advantage that it increases the effective water depth (Eq.(9)) improving the approximations discussed in Section 2.2.1.

3 Trough Moleai & Crocker proposed printing this device using a resin printer, however, these are less ubiquitous and more expensive than more conventional fused deposition printers[26,27]. Here a device was designed that could be printed with an Ultimaker S5[28] using PLA filament which is cheap and readily available.

The Moleai & Crocker device used a sharp circular outer perimeter to pin the fluid to be co-planar with

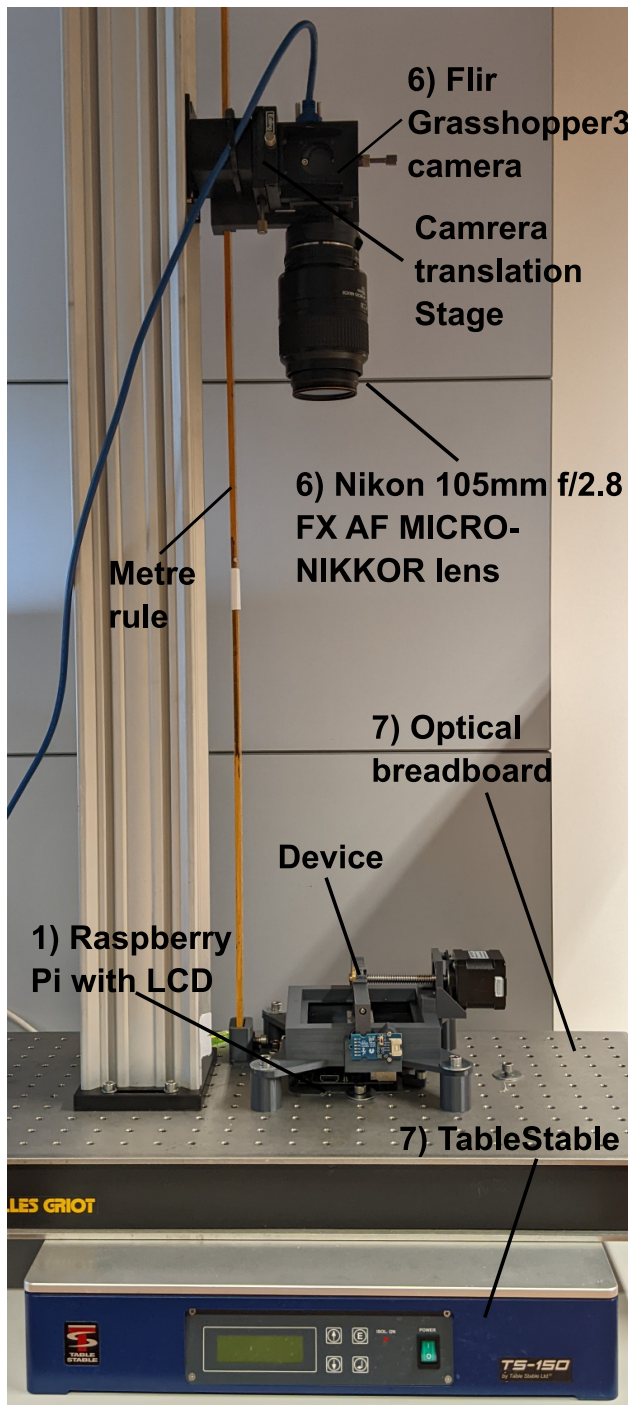


Figure 9: Annotated diagram of the apparatus. The apparatus would typically be covered, this has been omitted for the photograph. Cables have also been omitted.

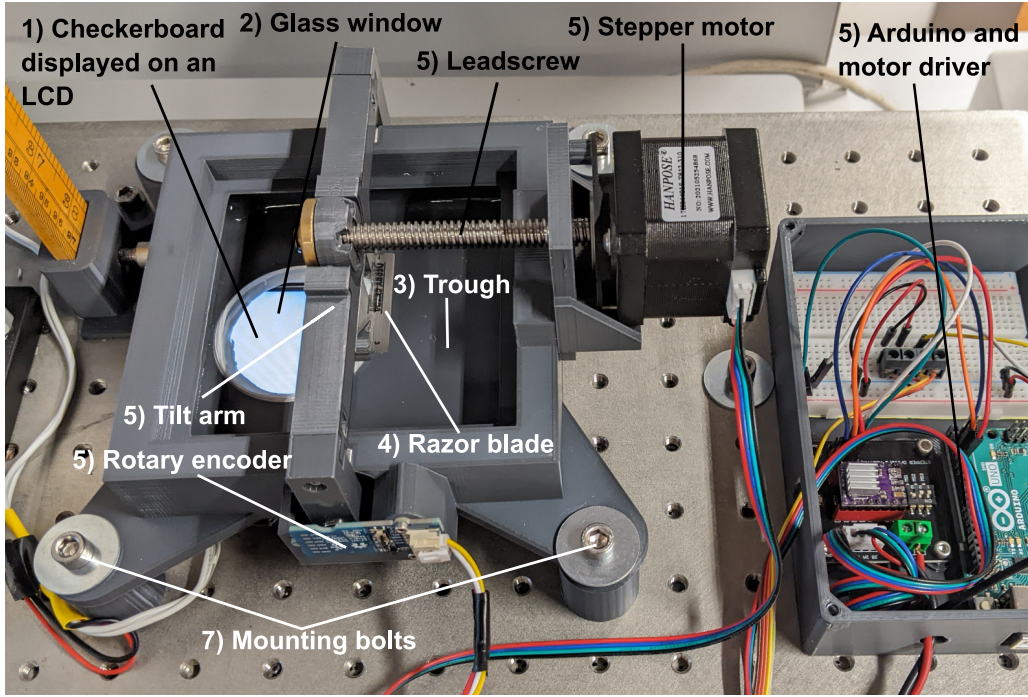


Figure 10: Diagram of the device with key components annotated.

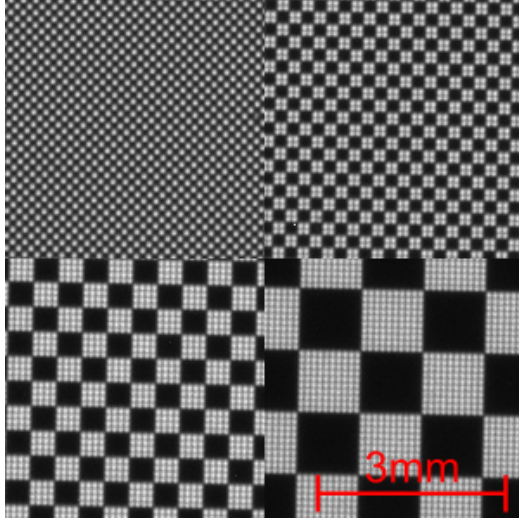


Figure 11: Photographs of different checkerboard sizes. From top left to bottom right: 1px, 2px, 4px, and 10px. Only the 2px used to collect data, see S.1.2.

the tilting interface. In this project, this boundary was moved many capillary lengths away from the tilting interface. This was done to reduce the effect of this boundary as it is not considered in the analytic solutions (see Appendix A) and to increase the precision with which the trough could be filled due to the larger overall volume.

4 Razor blade Moleai & Crocker's imaging method necessitated that the tilting interface was a

disk, see Fig.3. Resin printers allowed them to print these disks with the suitably sharp edges required for adequate pinning of the fluid. On a filament printer, this was not possible. However, imaging from above permits a straight edge to be used. This has several advantages. Firstly, the analytic solutions require fewer approximations, and second, a commercially available razor blade could be used. A straight-edge has the additional challenge compared to a disk of ensuring that the blade edge is parallel to the tilt axis. This was done by printing geometry to index with the geometry of the blade, as shown in Fig.12. For the razor used here $w = 11.0 \pm 0.1\text{mm}$.

5 Electronics One limitation of the Moleai & Crocker device was the inability to easily vary the angle of tilt. I improve this using a stepper motor with a leadscrew[29] and a rotary encoder[30], both controlled with an Arduino[31]. The razor blade was connected to a tilt arm supported by two bearings. A nut embedded in this arm connected it to the leadscrew. This nut was mounted on a flexible joint so that the arm pivoted as the motor turned. This works only in the limit of small angles, although, in practice $\pm 20^\circ$ was achievable. This method leads to strain in the tilt arm making the bearings necessary.

The tilt angle was measured using a magnetic rotary encoder[30]. This measured the rotation of a diametrically magnetised magnet mounted in the tilt arm along the axis of rotation. The encoder output was discretised into steps of 0.087° . This was the limiting factor in the tilt precision achievable

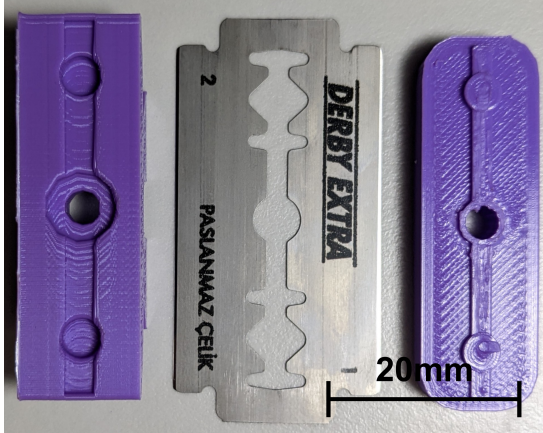


Figure 12: Photograph of the razor blade and the 3D printed parts used to align and attach it to the main device. A bolt would pass through the central holes to hold the assembly together.

however this was not a concern for the results of this experiment.

6 Camera and lens A large focal length lens was used. This allowed the camera to be placed further from the interface while retaining a high resolution in the region of interest. As discussed by Moisy et al.[14] this improves the small-angle approximations made and was tested in Section S.1.4. A fast shutter reduces the blur in the image and therefore increases the contrast of the carrier peaks found in the Fourier space. Unfortunately, this reduces the averaging over small vibrations and noise that a longer exposure would allow. To compensate many images should be taken to reduce the influence of noise. The lens aperture was kept small² to keep the checkerboard in focus as the tilting interface was raised.

7 Foundations The device, camera support, and Raspberry PI were independently mounted to an optical breadboard. This was to ensure there was no movement between the reference image and subsequent images as necessitated by FCD. The breadboard was placed on a TableStable[32], this both auto-levelled the device and reduced vibrations.

3.2 Scale calibration

To produce metric results, it is necessary to convert the pixel measurements into millimetres. Conventionally this is done by imaging and subsequently measuring an object of known dimensions[10]. This was attempted but found to be insufficient. The final method devised was to use the checkerboard itself. The separation of the carrier peaks in Fourier space

can be correlated to the checkerboard size if the size of an individual pixel on the LCD³ and the number of pixels per checkerboard are known. Unlike taking measurements from a reference object this can measure across the whole image simultaneously. This can also be done quickly and automatically reducing setup time. This method was found to be very robust and worked for a range of different checkerboard sizes and camera heights, see Sections S.1.2 to S.1.4.

4 Results and discussion

4.1 Fitting data to theoretical predictions

Images were collected for various tilt angles and then analysed using FCD (see Section 2.2); details of the data collection method are in Appendix B. The resultant surfaces are shown in Fig.13. The vertical scale in these plots has been approximated by taking approximate measures for the values in Eqs.(7) and (9), which gives maximum heights within 6% of the predicted value of, $w \sin(\alpha)$. Accurate tests of this value cannot be made as the surface near the blade cannot be imaged.

The predicted analytical solution (Eq.(3)) was fitted to these surfaces. This equation would predict two degrees of freedom; the vertical scaling discussed in Section 2.2.1 and the capillary length. During this process, it was discovered that it was also necessary to include the three rotational degrees of freedom, see Appendix A. This primarily accounted for the orientation of the camera, although other factors may have had similar effects, such as, if the glass window or screen was not parallel to the un-perturbed interface.

Fig.14 shows plots of the difference between the FCD surface and fitted surface measured as a percentage of the maximum height. Fig.14a shows the theoretical model provides an extremely good fit for the shape of the curve obtained. This can be seen from the mottled effect showing little systematic differences and only smaller random effects. The large maximum error observed in Fig.14a of 5.2% of the maximum height of the surface is due to the limited vertical precision of FCD. While Fig.14c shows a poorer fit the exponential solution is still accurate to within 3%. Comparing the first-order solution to the full solution (see Appendix A) the true surface would be expected to decay faster than the first-order exponential. This would lead to the large central region of disagreement seen in Fig.14c, the effect of this is discussed in Section 4.2.

²Here f/22.

³Taken from the datasheet[23].

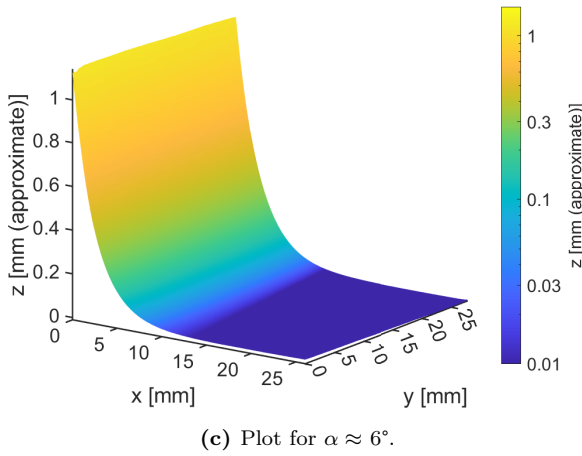
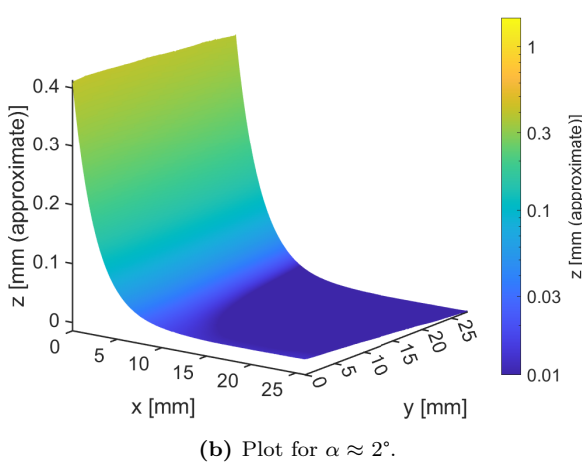
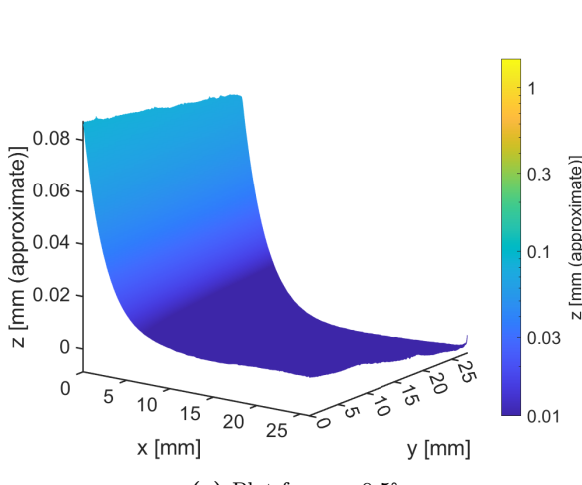


Figure 13: Plots of the surfaces calculated by FCD for three different tilt angles. The vertical scale has been approximated using Eqs.(7) and (9) using standard values for the optical indices.

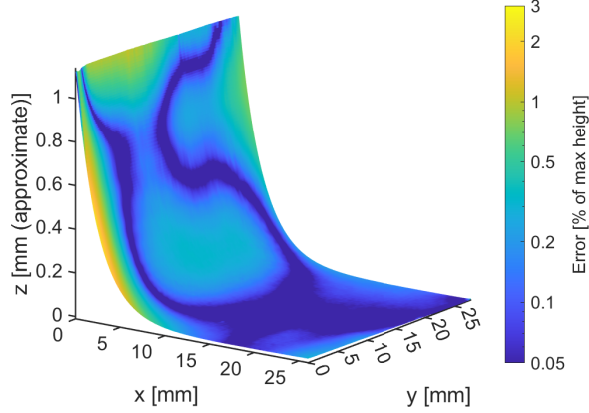
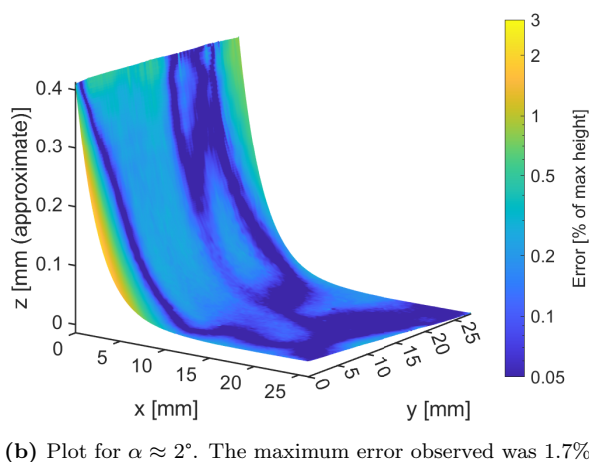
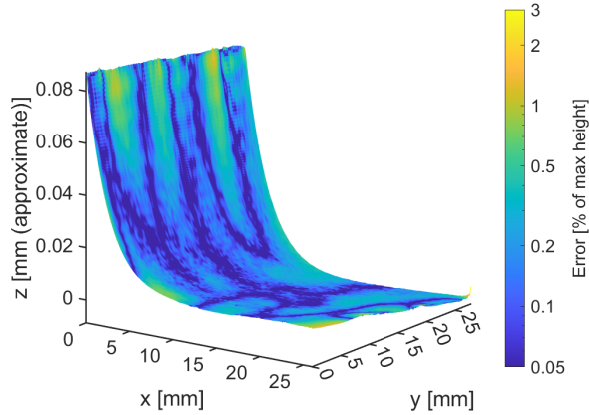


Figure 14: Plots of the surfaces shown in Fig.13 coloured to show the difference between the experimental surface and the first-order solution normalised to the maximum height of the surface so comparisons can be made between them. The large disagreement along the left and to a lesser extent right edge may be explained by the edge effects near the corner of the razor blade.

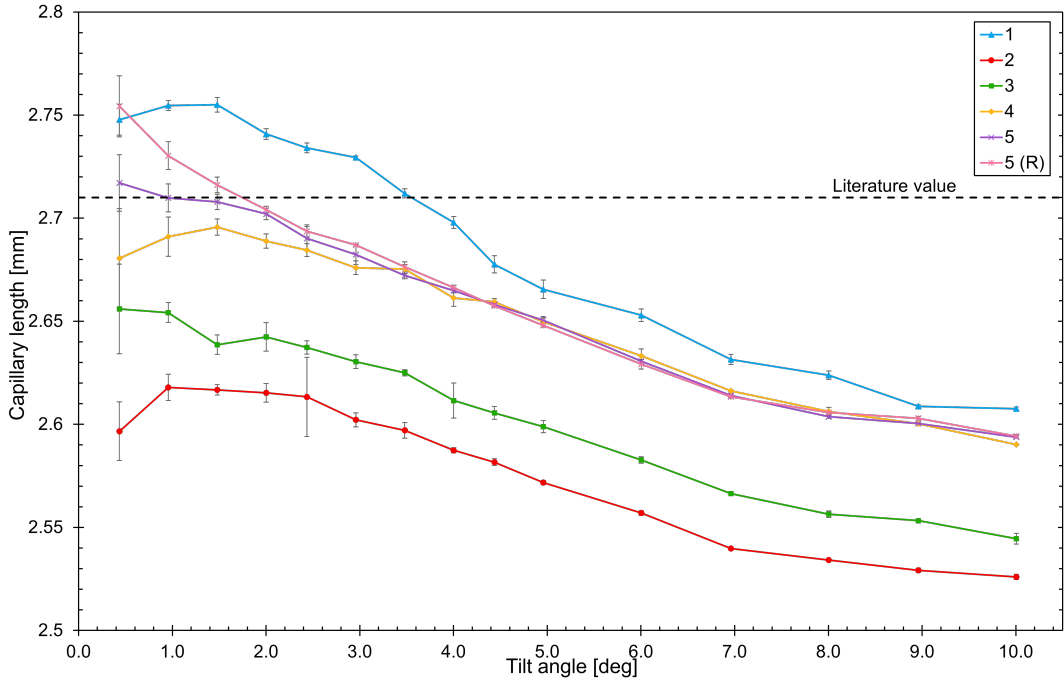


Figure 15: Plot of the fitted capillary length for five different fillings of the trough. Also plotted is the line of the fifth filling as the tilt angle returned to zero. All fillings show a similar downward trend in the capillary length but with initial systematic differences. Errors in the tilt angles are $\pm 0.04^\circ$ but may have a small systematic offset caused by the setup and alignment of the device. However, this offset would be expected to be consistent across the runs plotted here.

4.2 Precision of the device

Many tests were performed to examine the reliability and precision of the device. Here I discuss the most important limitations found. The other tests performed are contained in S.1.

To measure the capillary length of water FCD was performed for multiple tilt angles and multiple runs. For each run, the trough would be refilled and a new reference image taken, the results are shown Fig.15. Differences were observed in the fitted capillary length between photographs of the same interface, taken 1s apart. The error in each datum of Fig.15 was quantified by analysing these subsequent images. These were small random errors typically of the order of $\pm 0.003\text{mm}$. However, the limiting error was the systematic differences between runs, see Fig.15. The capillary length for each run likely varies due to small differences in the reference images. All subsequent images of a particular run are compared to this reference, hence, explaining the systematic nature of these differences.

I investigated explanations of these deviations. One possible cause would be the pinning of the interface to the blade's edge. This was tested by cycling the angle several times. While this was observed to cause changes in the measured capillary length for small angles, no general systematic error was observed such as in Fig.15, see Appendix C for details.

Another possible reason for the deviation between sets is the scale calibration method used. Comparing the reference images for each run and calculating conversion, small differences were observed. However, these were approximately a hundred times smaller than the deviations seen in Fig.15, so is not likely the primary source of the error.

A likely source of the error was the initial fill volume of the trough as this was done by eye separately for each run; different fill volumes would cause distortions in the reference image due to the non-planar interface that would be created. This distortion can also be observed in the symmetry of peaks in the Fourier domain similar to that shown in Fig.8d. This asymmetry can then be used as a measure of the fill volume, see Appendix D. Comparing the reference images of each run, showed run 5 has the lowest asymmetry, which would agree with this line being closest to the true value Fig.15. However, runs 1 and 2 appeared to have extremely similar symmetries suggesting the fill volume does not have a direct effect on the capillary length measured, implying more work needs to be done here to fully explore this method and determine the true source of the differences observed in Fig.15.

Fig.16 is the average over the runs in Fig.15. The downward trend in the capillary length while not predicted by the Laplace-Young equation is expected due to the first-order functions being fitted to the data, as discussed in Section 4.1. To test this

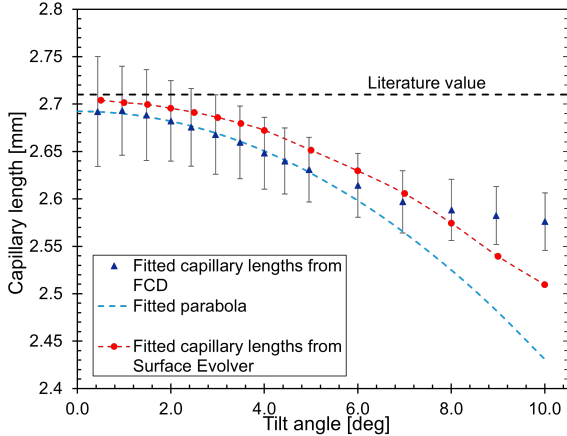


Figure 16: Plot of the fitted capillary length for different tilt angles averaged over the five fillings shown in Fig.15. Also plotted are capillary lengths found by fitting the same solution to surfaces with a capillary length of 2.71 mm generated by Surface Evolver[9] and a parabola that was fitted to FCD data for angles less than 5°.

surfaces were generated using Surface Evolver[9] for multiple tilt angles, with a capillary length of 2.71 mm. Then Eq.(3) was fitted to a cross-section of this surface. The resultant fitted capillary length decreased with the tilt angle (within the region of interest) with this behaviour being well modelled by a parabola, these results are plotted in Fig.16. On this basis, a parabola has been fitted to the data in Fig.16, below 5°. These lines appear to agree within the error although the FCD data appears to initially decay faster than the Surface Evolver data. This is likely due to this decay being dependent on the other parameters such as the pinning edge's distance to the pivot axis which will in truth differ between the simulation and the device.

The poor fit of the parabolic solution at higher angles is most likely due to a breakdown in the approximations made in Section 2.2. Crucially the angle of the normal to the surface can no longer be considered small and the overall height change is also no longer small for larger angles. Both of these approximations would lead to the calculated height of the surface being reduced for the region closest to the blade, hence yielding larger capillary lengths than expected. This leads to the conclusion of an ideal tilt angle. Figs.14 and 15 show the largest individual errors are for the smaller tilt angles. This is precisely what was observed by Moleai & Crocker, see Section 1.2.2. While large angles are poorly approximated by the method used here. Here the ideal range is roughly 2-4° which corresponds to between 2.5-5% of the overall water height.

From Fig.16 the capillary length of water is measured as $2.69 \pm 0.05\text{mm}$, which is in good agreement with the literature value of $2.71 \pm 0.01\text{mm}$ at the lab

temperature of between 21 and 24°C. This value was calculated from surface tension measurements taken by Vargaftik et al.[33] together with air and water density estimates from Kaye & Laby[34].

5 Conclusions

I have demonstrated that a 3D printed device can be constructed which creates a fluid interface that can be measured using fast checkerboard decomposition. Further, I have shown that this device can be used to measure the capillary length of water. Several limitations were discovered, principally that the initial conditions play a critical role in the final values measured. Given this limitation, a value of $2.69 \pm 0.05\text{mm}$ was obtained which is in agreement with the literature value. However, if this limitation could be removed, surface tension values to a precision of $\pm 0.2\text{mN m}^{-1}$ would be achievable based on the errors seen between different photographs of the same interface, this precision would be of the order of more traditional methods.

Primarily, I was able to show that an LCD can be integrated with FCD and indicated some of the many advantages this may provide over a printed method. This was in addition to showing that using the checkerboard to perform the scale calibration was an adequate and dependable method of scaling the data. This investigation has also shown the limited ability to apply first-order approximations to a tilting straight edge and therefore the need for more complex analysis to be performed to make better use of the larger surface deformations achievable with this device.

6 Further work

Some of the decisions made in this project were made in the interest of time and the development of this device would benefit from a longer investigation. With limitations of the device and method being reducible with further work.

In particular, the data collected shows regions, where the approximations made, fail. It would therefore be instructive to analyse this data differently. Possible approaches would be to use a different integration method for calculating, $h(x, y)$ such as the newton iteration used in other work[12, 13]. It would also be possible to take an approach similar to Moleai & Crocker[6] fitting numerical solutions to the data collected. Both of these approaches would benefit from more computational resources than those used in this project but would be instructive to how the device and methodology could be improved and would not require more data to be taken.

Following this investigation, I would primarily explore the idea of using the Fourier domain skew

to help set up the fill volume as discussed in Appendix D. I would also want to experiment with some different aspects of the device including adjusting the thickness of the glass window and water depth, as examples. There are also several smaller improvements I would like to make, such as improving the integration between the tilt control and camera, so the device could take data more autonomously. Finally think it would be fascinating to continue exploring the applications of using an LCD for FCD, for example, by taking advantage of colour.

Acknowledgements

I would like to thank my supervisor; Prof. Pietro Cicuta for all of his help, inspiration, and ideas throughout the project. I would also like to thank Dr. Jurij Kotar, Samuel McDermott, and Jeppe Klitgaard for their generous contributions, supplying hardware and technical support. A special thanks to Prof. Dominic Vella for discussing his solutions with me.

References

- [1] M. Steinhart, “Physics and chemistry of interfaces. by hans-jürgen butt, karlheinz graf, and michael kappl.,” *Angewandte Chemie*, vol. 116, p. 7, 07 2004.
- [2] J. B. Wade, “Chapter 1 - physicochemical principles governing agglomeration and growth kinetics,” in *Handbook of Pharmaceutical Wet Granulation* (A. S. Narang and S. I. Badawy, eds.), pp. 3–35, Academic Press, 2019.
- [3] R. L. Sakaguchi and J. M. Powers, “Chapter 4 - fundamentals of materials science,” in *Craig’s Restorative Dental Materials (Thirteenth Edition)*, pp. 33–81, Saint Louis: Mosby, thirteenth edition ed., 2012.
- [4] B. Gupta and A. Moghe, “2 - nanofiber structures for medical biotextiles,” in *Biotextiles as Medical Implants* (M. W. King, B. S. Gupta, and R. Guidoin, eds.), Woodhead Publishing Series in Textiles, pp. 48–90, Woodhead Publishing, 2013.
- [5] E. A. Guzzi, H. Ragelle, and M. W. Tibbitt, “Surface tension-assisted additive manufacturing of tubular, multicomponent biomaterials,” in *Methods in Molecular Biology*, pp. 149–160, Springer US, Aug. 2020.
- [6] M. Molaei and J. C. Crocker, “Interfacial microrheology and tensiometry in a miniature, 3-d printed langmuir trough,” *Journal of Colloid and Interface Science*, vol. 560, pp. 407–415, 2020.
- [7] G. Soligno, M. Dijkstra, and R. van Roij, “The equilibrium shape of fluid-fluid interfaces: Derivation and a new numerical method for young’s and young-laplace equations,” *The Journal of Chemical Physics*, vol. 141, no. 24, p. 244702, 2014.
- [8] J. Drelich, C. Fang, and C. White, *Measurement of interfacial tension in Fluid-Fluid Systems*, pp. 3152–3166. Encyclopedia of Surface and Colloid Science, 01 2002.
- [9] K. A. Brakke, “The surface evolver,” *Experimental Mathematics*, vol. 1, no. 2, pp. 141–165, 1992.
- [10] J. D. Berry, M. J. Neeson, R. R. Dagastine, D. Y. Chan, and R. F. Tabor, “Measurement of surface and interfacial tension using pendant drop tensiometry,” *Journal of Colloid and Interface Science*, vol. 454, pp. 226–237, 2015.
- [11] A. C. Merrington and E. G. Richardson, “The break-up of liquid jets,” *Proceedings of the Physical Society*, vol. 59, pp. 1–13, jan 1947.
- [12] Z. Liu, X. Huang, and H. Xie, “A novel orthogonal transmission-virtual grating method and its applications in measuring micro 3-d shape of deformed liquid surface,” *Optics and Lasers in Engineering*, vol. 51, no. 2, pp. 167–171, 2013.
- [13] W. Shi, X. Huang, and Z. Liu, “Transmission-lattice based geometric phase analysis for evaluating the dynamic deformation of a liquid surface,” *Opt. Express*, vol. 22, pp. 10559–10569, May 2014.
- [14] F. Moisy, M. Rabaud, and K. Salsac, “A synthetic schlieren method for the measurement of the topography of a liquid interface,” *Experiments in Fluids*, vol. 46, pp. 1021–1036, Jan. 2009.
- [15] S. Wildeman, “Real-time quantitative schlieren imaging by fast fourier demodulation of a checkered backdrop,” *Experiments in Fluids*, vol. 59, May 2018.
- [16] L. Huang, C. S. Ng, and A. K. Asundi, “Dynamic three-dimensional sensing for specular surface with monoscopic fringe reflectometry,” *Opt. Express*, vol. 19, pp. 12809–12814, Jun 2011.
- [17] H. Murase, “Surface shape reconstruction of an undulating transparent object,” in [1990] *Proceedings Third International Conference on Computer Vision*, pp. 313–317, 1990.
- [18] M. Zhong, X. Huang, H. Dong, and Z. Liu, “3d shape measurement of complex transparent liquid surfaces using monoscopic deformed fringe transmissometry,” *Measurement Science and Technology*, vol. 30, p. 115201, sep 2019.
- [19] M. Motamedi, “How digital image correlation (dic) technique works! (introduction to dic technique),” 12 2019.
- [20] J. Bush, *18.357 Interfacial Phenomena*. Massachusetts Institute of Technology, MIT OpenCourseWare, 2010.
- [21] V. P. A.I. Rusanov, *Interfacial Tensiometry*. Elsevier Science, 1996.
- [22] M. Anderson, A. Bassom, and N. Fowkes, “Exact solutions of the laplace–young equation,” *Proceedings of The Royal Society A: Mathematical, Physical and Engineering Sciences*, vol. 462, pp. 3645–3656, 12 2006.
- [23] “Hyperpixel 4.0 - hi-res display for raspberry pi.” <https://shop.pimoroni.com/products/hyperpixel-4?variant=12569485443155>. Accessed: 16/03/2022.

- [24] "What is a raspberry pi?." <https://www.raspberrypi.org/help/what-is-a-raspberry-pi/>, 2015. Accessed: 09/05/2022.
- [25] "50 gq 00 precision glass windows." <https://www.comaroptics.com/pdf/50%C2%A0GQ%C2%A000.pdf>, 2015. Accessed: 16/03/2022.
- [26] D. Roberson, "How much does 3d printing cost?." <https://ultimaker.com/learn/how-much-does-3d-printing-cost>, Sep 2022. Accessed: 21/03/2022.
- [27] "How much does a 3d printer cost?." <https://formlabs.com/blog/how-to-calculate-3d-printer-cost/>. Accessed: 21/03/2022.
- [28] "Ultimaker s5 specification sheet." <https://docs.rs-online.com/8d73/A70000006509368.pdf>, 2018. Accessed: 09/05/2022.
- [29] "Nema17 stepper motor with 31cm lead screw shaft." https://www.handsontec.com/dataspecs/motor_fan/lead-screw-motor.pdf, 2021. Accessed: 09/05/2022.
- [30] "As5600 12-bit programmable contactless potentiometer." https://ams.com/documents/20143/36005/AS5600_DS000365_5-00.pdf/649ee61c-8f9a-20df-9e10-43173a3eb323, 2020. Accessed: 16/03/2022.
- [31] "Arduino uno r3, product reference manual." <https://docs.arduino.cc/resources/datasheets/A000066-datasheet.pdf>, 2022. Accessed: 09/05/2022.
- [32] "Manual ts-150_ts-140_ts-300 v1.05." http://tablestable.com/uploads/ckeditor/TS-150/Manual%20TS-150_TS-140_TS-300%20V1.05.pdf, 2021. Accessed: 16/03/2022.
- [33] N. B. Vargaftik, B. N. Volkov, and L. D. Voljak, "International tables of the surface tension of water," *Journal of Physical and Chemical Reference Data*, vol. 12, no. 3, pp. 817–820, 1983.
- [34] G. W. C. G. W. C. Kaye, *Tables of physical and chemical constants and some mathematical functions / originally compiled by G.W.C. Kaye and T.H. Laby*. London: Longman, 14th ed. / now prepared under the direction of an editorial committee. ed., 1973.
- [35] M. C. Jones and A. Pewsey, "Sinh-arcsinh distributions," *Biometrika*, vol. 96, pp. 761–780, 10 2009.
- [36] S. Z. Can, C. F. Chang, and R. A. Walker, "Spontaneous formation of dppc monolayers at aqueous/vapor interfaces and the impact of charged surfactants," *Biochimica et Biophysica Acta (BBA) - Biomembranes*, vol. 1778, no. 10, pp. 2368–2377, 2008.
- [37] H. Dominguez, A. M. Smolyrev, and M. L. Berkowitz, "Computer simulations of phosphatidyl-choline monolayers at air/water and ccl4/water interfaces," *The Journal of Physical Chemistry B*, vol. 103, no. 44, pp. 9582–9588, 1999.
- [38] S. Li, L. Du, and W. Wang, "Impact of anions on the surface organisation of lipid monolayers at the air–water interface," *Environmental Chemistry*, vol. 14, p. 407, 01 2017.
- [39] J. Carrascosa-Tejedor, A. Santamaria, D. Pereira, and A. Maestro, "Structure of dppc monolayers at the air/buffer interface: A neutron reflectometry and ellipsometry study," *Coatings*, vol. 10, no. 6, 2020.
- [40] F. W. J. Olver, A. B. O. Daalhuis, D. W. Lozier, B. I. Schneider, R. F. Boisvert, C. W. Clark, B. R. Miller, B. V. Saunders, H. S. Cohl, and e. M. A. McClain, *NIST Digital Library of Mathematical Functions. Chapter: 10.40(i) Hankel's Expansions*. 2022. Accessed: 09/05/2022.

Appendices

Appendix A A solution to the Young-Laplace equation for a straight edge

Here we follow the derivation of the interface shape for a straight edge inclined at an angle, which was derived by Prof. Vella (Oxford) and bears resemblance to [22]. This problem can be considered in one dimension. Following the construction by Bush[20], the Laplace-Young equation in one dimension takes the form

$$\gamma \frac{h_{xx}}{(1 + h_x^2)^{3/2}} = \rho g h. \quad (\text{A1})$$

Writing in terms of the capillary length ($l_c = \sqrt{\frac{\gamma}{\rho g}}$), and multiplying by h_x the equation can then be integrated giving

$$1 - (1 + h_x^2)^{-1/2} = \frac{h^2}{2l_c^2}. \quad (\text{A2})$$

Writing the equation in dimensionless form so $H = h/l_c$ and rearranging for H_x

$$H_x^2 = \frac{1 - (1 - \frac{1}{2}H^2)^2}{(1 - \frac{1}{2}H^2)^2} = H^2 \frac{4 - H^2}{(2 - H^2)^2}, \quad (\text{A3})$$

so

$$H_x = -\frac{H\sqrt{4 - H^2}}{2 - H^2}. \quad (\text{A4})$$

This can be integrated using standard integrals. Using the boundary conditions; $H \rightarrow 0$ as $x \rightarrow \infty$ and $H = \frac{w \sin(\alpha)}{l_c}$ when $x = w \cos(\alpha)$ gives

$$\frac{x - w \cos(\alpha)}{l_c} = \sqrt{4 - H_{max}^2} - \tanh^{-1} \left(\sqrt{1 - \frac{H_{max}^2}{4}} \right) - \sqrt{4 - H^2} + \tanh^{-1} \left(\sqrt{1 - \frac{H^2}{4}} \right), \quad (\text{A5})$$

where $H_{max} = \frac{w \sin(\alpha)}{l_c}$. In the limit of $w \sin(\alpha) \ll l_c$, expanding to leading order this can be reduced to

$$\frac{x - w \cos(\alpha)}{l_c} = \frac{1}{4} (H^2 - H_{max}^2) - \ln \left(\frac{H}{H_{max}} \right). \quad (\text{A6})$$

When the first term is small this can be seen to reduce to the pure exponential decay which can be derived from the Poisson approximation to the Young-Laplace equation,

$$H = H_{max} \exp((w \cos(\alpha) - x)/l_c). \quad (\text{A7})$$

One of the crucial differences between the fuller solutions in Eqs.(A5) and (A6) and the pure exponential solution is that the former can account for the ability of the fluid surface to retreat under the boundary and become concave. This effect is expected to be observed for $H_{max} > \sqrt{2}$, this condition was never met during this project.

To fit this first-order solution to the data collected, it is necessary to first expand this to a 2D surface and then consider the three rotational and 3 transitional degrees of freedom; together this results in the fitting equation of

$$h(x, y) = A \cos(\omega_x) \cos(\omega_y) \exp \left(\frac{\cos(\omega_z)x + \sin(\omega_z)y}{l_c} \right) + \sin(\omega_y)x + \sin(\omega_x)y + C. \quad (\text{A8})$$

The parameters used are discussed in Table A1. One of the remaining translational degrees is incorporated into A while the other is removed by the symmetry of a straight edge.

Parameter	Meaning
A	Vertical scaling
l_c	Capillary length
C	z translation
ω_x	x rotation
ω_y	y rotation
ω_z	z rotation

Table A1: The fitting parameters used in Eq.(A8)

Appendix B Data acquisition & methodology

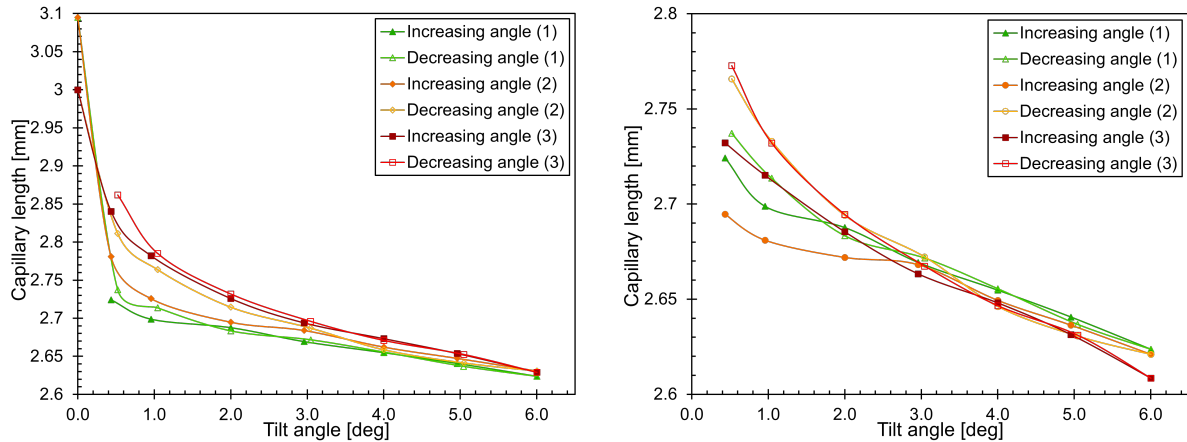
Here I present the experimental method I used to collect data.

1. First, the trough must be prepared.
 - (a) Initially, the trough was filled with distilled water for a minimum of 12h to reduce the effect that any contaminants in the PLA might have on measurements. This was also done while the apparatus was not in use to keep the trough clean. This water should be thoroughly removed before taking measurements. Components other than the trough should not be submerged in water for long periods as this will cause swelling and the part would need to be scrapped.
 - (b) Next, the trough should be levelled, in this project this was accomplished using the TableStable with an auto-levelling feature.
 - (c) Then, the zero position must be set for the tilt arm. It was important to do this regularly, for example, if the tilt arm or other component is exchanged or replaced. Although this is not necessary for every set of data taken. This was most easily done using a spirit level placed on the tilting interface itself. To do this the leadscrew was turned manually until the spirit level was level. The output of the rotatory encoder for this level position was then used as the zero position. This method was found to be accurate to $<0.2^\circ$. Once calibrated this zero position was easily returned to a high degree of accuracy using the encoder and motor.
 - (d) Next, the camera's focal length and aperture should be set.
 - (e) The final step of preparation is to align the entire device so that the edge of the blade is parallel to the edge of the camera's view. After this is done the trough is bolted down.
2. Once prepared the trough was filled with water taken from a Millipore Biopak polisher. The method utilised here was to slightly under or overfill the trough then with a small syringe, then add or remove water until the interface was with the blade. This was found to be easiest when done under a bright light.
3. The next step is to crop the region of the camera's view that is captured. This is done to ensure that only the checkerboard is imaged. To do this the field of view was cropped so that the blade's edge is just out of view. This must be done when the tilt arm is at the zero position. This is why the edge was made parallel to the camera's view earlier. The other three edges are set so that only the underlying checkerboard can be seen in the cropped image's view. This completes the setup procedures. At this stage, the camera's shutter speed, frame rate etc. should be set. Options such as gain and exposure should be set so that these will not change during the rest of the experiment.
4. Once set up, the apparatus should be covered to reduce the influence of the lab lights or other stray light sources.
5. The next step is to take the initial reference image(s).
6. Following this data can be taken. For each data point, e.g. each tilt angle, several photographs should be taken. Typically this would be between 3 and 10 photographs taken 1s apart. This delay is to help reduce the effect dust and small particulates may have on the result. These surface contaminants seem unavoidable but taking photographs delayed by 1s or more mean the particulates move and so do not cause a constant effect.
7. Once one set of data was collected, the device was reset using the same procedure above before taking another set, using a vacuum pump to remove the water between runs. This should be repeated several times to reduce the effect of any excess volume. Between runs, the tilting interface is reset to the zero position in-order to take the reference image again.

8. Data taken was then processed using a MATLAB script where the initial steps were to perform the FCD analysis followed by integrating the displacement field to get the heightmap. Much of this code was adapted from the code written by Wildeman[15].
9. The result of the FCD was then fitted to the predicted surface and the fitting parameters extracted. Errors were quantified with the different parameters between photographs as these were significantly larger than the errors in the fitting parameters themselves.

Appendix C Pinning & hysteresis

The results of this experiment are possibly limited by the quality of the pinning of the surface to the edge of the razor blade. This was tested by measuring the capillary length as the tilt angle was cycled to 6° and back to 0° three times. Fig.C1a shows the results. The measured capillary lengths at 0° are dramatically different to the other lengths and are effectively meaningless. This is because while the surface constructed by FCD was not flat, as might be expected, it showed no meaningful exponential shape and can therefore be mostly attributed to noise thus resulting in wildly different capillary lengths. The rest of the data does show a trend with a general increase in the capillary length overtime for small angles but a good amount of consistency at higher angles. This does indicate the pinning of the surface remains fairly consistent. For Fig.C1a a single reference image taken at the beginning was used for all subsequent FCD. Fig.C1b however, shows the same data where the previous image for a tilt angle of 0° was used as the reference image. While the trend of increasing capillary length was observed, the data has become significantly tighter grouped. This implies the significant role that the reference image has and the importance of controlling it.



(a) Plot of how the fitted capillary length changes while cycling the tilt angle. Error bars have been omitted for clarity but can be assumed to be approximately ± 0.005 mm. The dramatically different values at 0° are due to the calculated surface not being well modelled by Eq.(A8), indicating the precision that the zero position can be returned to. Overall this shows an increase over each cycle.

(b) Plot of the same data in Fig.C1a but where the photos taken at 0° have been used as the reference images for the next cycle. The data shows a considerable amount more agreement. This does indicate the level of importance that the reference image plays in this analysis. Error bars have been omitted but are approximately ± 0.005 mm.

Figure C1: Plots of how the measured capillary length changes while cycling the tilt angle three times.

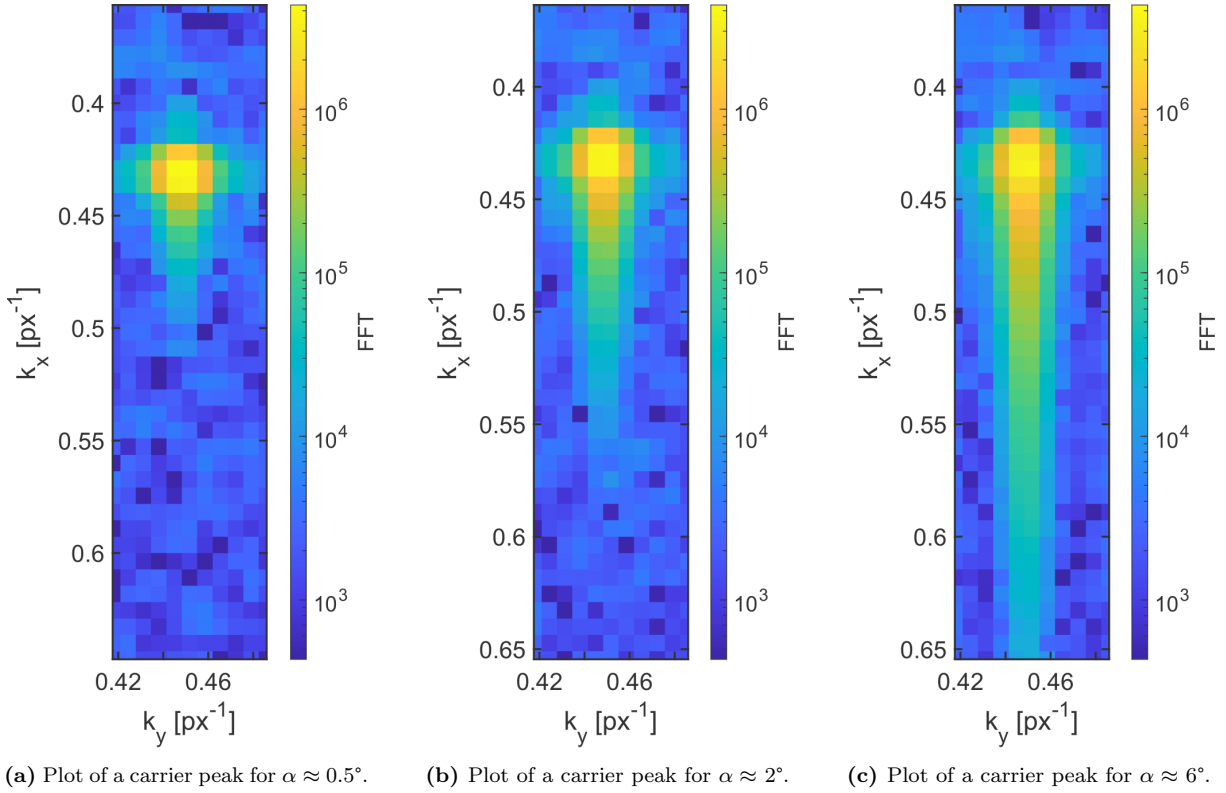


Figure D1: Plots of the carrier peaks for different tilt angles, showing the increase in tail length with increasing angle. The same effect is observed for different filling volumes.

Appendix D Determination of fill volume from Fourier domain

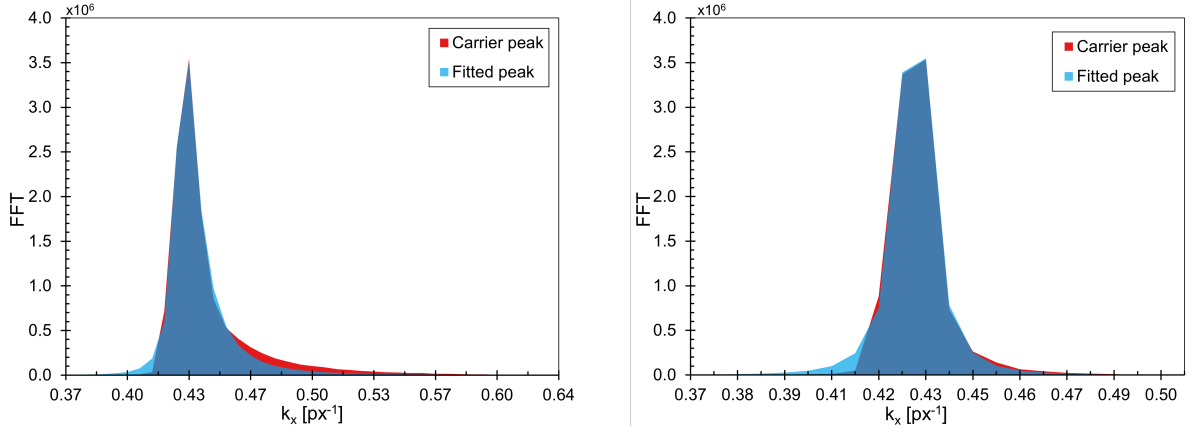
Here I test the hypothesis that the water volume can be determined from the form of the carrier peaks in the Fourier domain. Different filling levels and tilt angles lead to the carrier peaks becoming highly asymmetric, as shown in Fig.D1 whereas the tilt angle was increased the tail of the peak grew longer. Without mathematical justification, the function in Eq.(D1) was fitted to these peaks. This is a modified form of Johnson's SU distribution[35] for the k_x direction, the direction of the majority of the skew. A conventional Gaussian is fitted to the k_y direction.

$$FFT(k_x, k_y) = A \exp \left(-\frac{1}{2} \left(S_f + \sinh^{-1} \left(\frac{k_x - c_x}{\sigma_x} \right) \right)^2 - \frac{1}{2} \left(\frac{k_y - c_y}{\sigma_y} \right)^2 \right), \quad (D1)$$

With the fitting parameters in Table D1. This form was chosen as S_f (skew factor) directly changes the skew of the peak in a similar way to the peaks observed from the data. A skew in the positive k_x direction gives a negative skew factor and vice versa, with $S_f = 0$ producing a symmetric peak. To test if the fill level could be detected in this way the trough was partially filled and imaged after each addition of 0.5 mL until the trough was visibly overfilled then doing the same on the removal of 0.5 mL increments. By fitting Eq.(D1) to the carrier peaks the skew factor was found, example plots are shown in Fig.D2. This is plotted in Fig.D3. This shows that it is possible to measure the fill level with this method. While the fill and return lines don't overlap this is most likely due to limitations in the precision with which water was added and removed.

Also plotted are the skew factors from the reference images taken while collecting the data in Section 4.2. This shows that the data collected for runs 4 and 5 had the lowest initial skew of the five runs taken. This would agree with these runs having the capillary length closest to the literature value. However, all skew factors are positive and show little overall variation considering the standard deviation in the skew factor each run is ± 0.1 . Therefore, there does not appear any direct correlation between the skew factor measured and the capillary lengths. Specifically, lines for runs 1 and 2 are extremely similar but have the largest differences in capillary lengths, see Fig.15. For this reason, there would need to be more work

Parameter	Meaning
A	Vertical scaling
c_x	k_x translation
c_y	k_y translation
σ_x^2	k_x variance
σ_y^2	k_y variance
S_f	Skew factor

Table D1: Fitting parameters used in Eq.(D1)(a) Peaks for the initial fill (0 mL on Fig.D3). Fitted peak has a skew factor of -0.48 ± 0.04 .(b) Peaks for the minimum skew observed in Fig.D3 (3 mL). Fitted peak has a skew factor of -0.025 ± 0.013 .**Figure D2:** Profiles of the carrier peaks in the k_x direction. Overlaid is the corresponding fitted peak. This shows the reasonable fit produced, however the poor fit on the left side of both plots indicates a better fitting function or technique may be beneficial.

done in this area to make more conclusive results. The data here would suggest that I filled the trough consistently over by 4 – 5mL. A more likely reason is that the zero tilt position of the blade was different between this filling data and the capillary length data, as this would be expected to have a similar effect to the fill volume. However, this data does suggest the consistency that the trough was filled is <0.5 mL corresponding to ≈ 0.08 mm of fill height.

The function fitted here does not match the observed peaks precisely as shown in Fig.D2, it is, therefore, possible that a different function would yield different results, however, the data collected does show the principle of performing this type of analysis and could in principle be used to ensure the filling of the trough is consistent between runs. The idea of analysing the data in this way was only conceived towards the end of the project and so there was insufficient time to collect data that was adequate to make any definitive conclusions or to use this approach to improve the other data collected such as in Section 4.2 and Appendix C. This would be one of the primary focuses of the project moving forward.

During this process, many of the other parameters such as the variance in k_x and k_y and the position of the peaks themselves were tested to attempt to find a relationship between the parameter and the fill volume with little success. Other functions similar to Eq.(D1) such as a skew Gaussian and the Landau distribution were also tested but yielded less meaningful results.

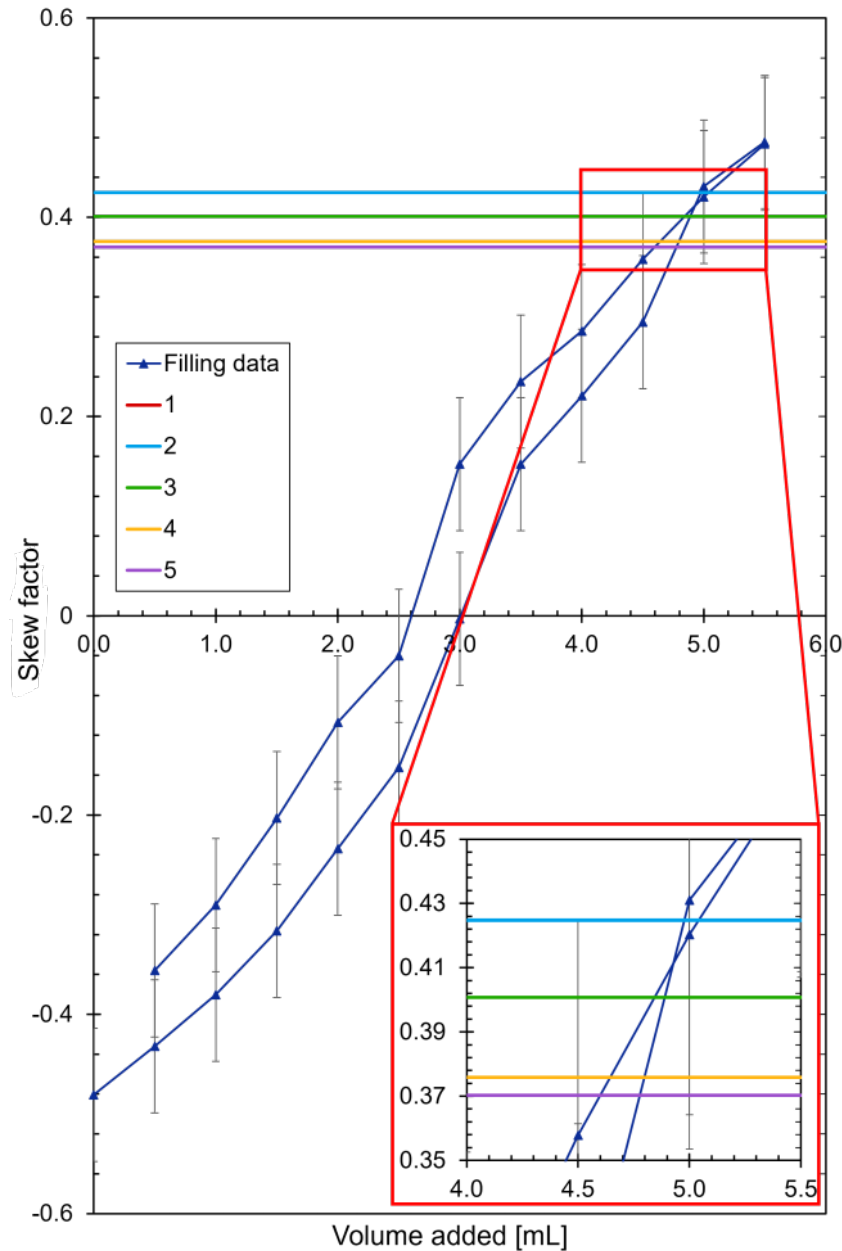


Figure D3: Plot of how the skew factor changes with the filling of the trough. This was taken while filling and then emptying the trough from an initial under-filled volume. Deviations in these lines are very likely the result of the errors accumulated in the filling volumes. The line for run 1 is precisely behind the line for run 2, so cannot be seen.

Supporting tests and data for
Interfacial tensiometry using checkerboard decomposition, a sharp tilting edge, and a 3D printed trough

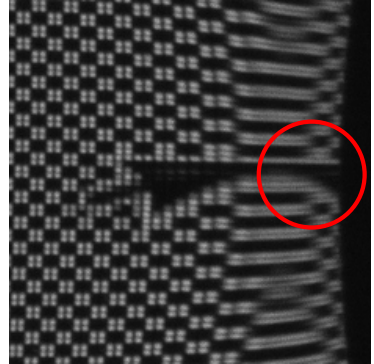
BGN: 8266X

May 16, 2022

S.1 Tests of the device

S.1.1 Negative tilt angles

Throughout the project, I only considered positive tilt angles so that the interface was raised above the undisturbed surface. This was a deliberate choice. As shown in Section S.1.1 negative tilt angles lead to ray crossings (see Moisy et al.[14]) and therefore what appears like reflections of the checkerboard, here seen as a reflection of the Raspberry PI's mouse. This effect was not observed for positive angles. This demonstrates an advantage of using the LCD as this effect could be easily detected by changing what was displayed. While negative angles were tested and it was found that it was possible to recover the surfaces, because of this ray crossing and simply to limit the scope of this investigation, these angles were not tested in detail.



S.1.2 Checkerboard size

Using the LCD the checkerboard's size and position can be changed without changing the other parameters of the experiment. Critically, without needing to change the filling of the trough.

To test checkerboard size, five checkerboards were used with each checkerboard square measuring 1,2,3,4, and 10px¹. Examples are shown in Fig.11. The capillary lengths for each checkerboard size for different tilt angles are shown in Fig.S2. While there were small differences between each of the sizes, in general, there is good agreement between them, including a small systematic offset to the literature value of the capillary length. This does emphasise the inaccuracies of the fitting procedure at small angles. The poor agreement of the 10px line is expected due to the lower resolution possible for the larger grids. While the 1px line does show good agreement with the other lines, the FCD failed at angles above 4°. While did not consistently occur, it does show a limitation of using a checkerboard that is too fine for the camera's resolution. For this camera distance, each LCD pixel measured approximately 3.6 camera pixels. Hence, a 1px grid is at the limit of Nyquist's theorem[15] so would not be expected to produce consistent results. It is for this reason, that throughout this investigation 2px were used. Fig.S2 also shows the robustness of using the checkerboard to calculate the metric conversion as little systematic error was observed.

Figure S1: Photo of the Raspberry PI's mouse and its effective reflection (circled) caused by rays crossing as a consequence of the interface shape.

S.1.3 Checkerboard translations

Four of the eight unique pixel translations of a 2px checkerboard were tested for systematic differences. This data was collected using an identical method to data collected in Section S.1.2 except the checkerboard was translated for each set. Fig.S3 shows measured capillary lengths against different angles for each of the translations. This shows no significant systematic differences observed indicating that the specific position of the checkerboard does not need to be considered; this was repeated. In some runs (Fig.S3) differences were observed, however, these were not reproducible. This may indicate that the translation does have a small effect and would likely be more pronounced for a larger checkerboard size. However, because a 2px checkerboard was used for the majority of the data collected during this investigation the same was used here. The systematic differences observed here are smaller than those observed elsewhere so this wasn't considered further.

¹Approximately 0.1,0.2,0.3,0.4, and 1mm.

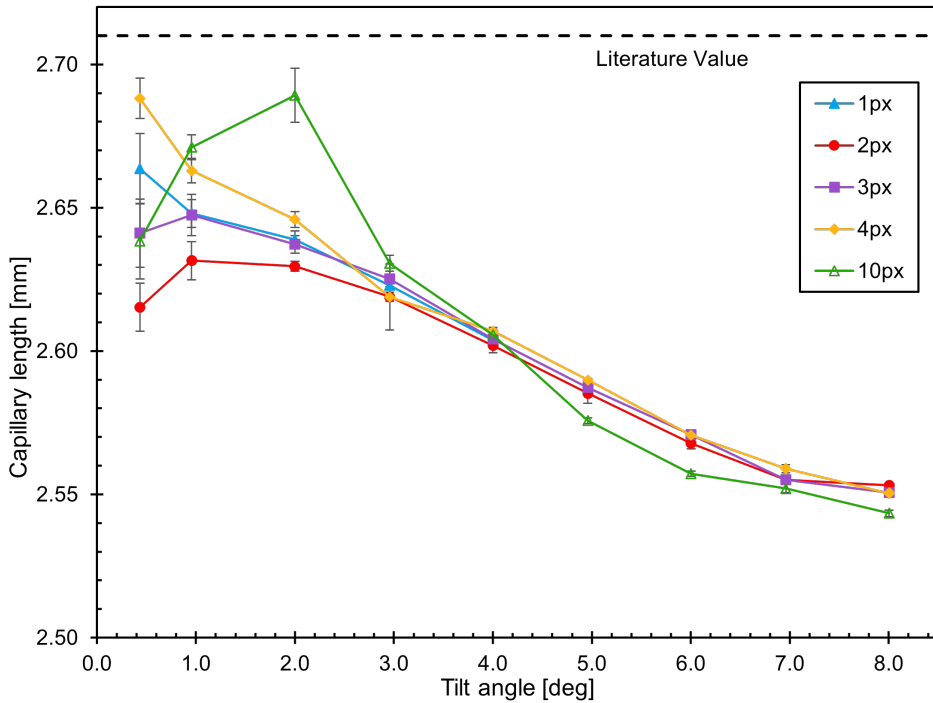


Figure S2: Plot of the fitted capillary length for different sizes of checkerboards. This shows an upper limit on the size of less than 10px. Otherwise, all of the checkerboards show a high degree of agreement all with the same systematic difference to the literature value. All curves show the same decrease in the fitted capillary length versus angles. The disagreement at small angles is somewhat expected due to the generally poor precision in this region.

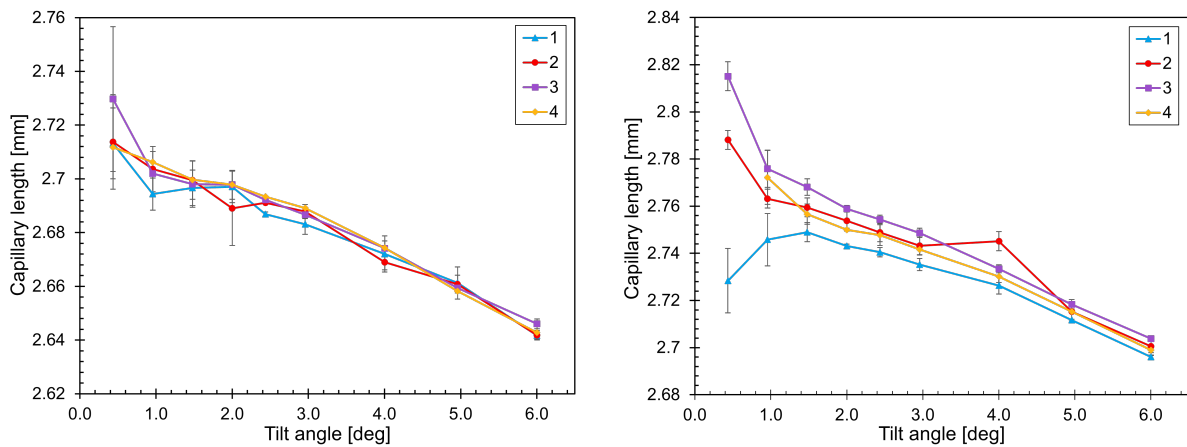


Figure S3: Plots of four different checkerboard translations. Two different sets have been taken. These show little systematic difference that is consistent between these runs.

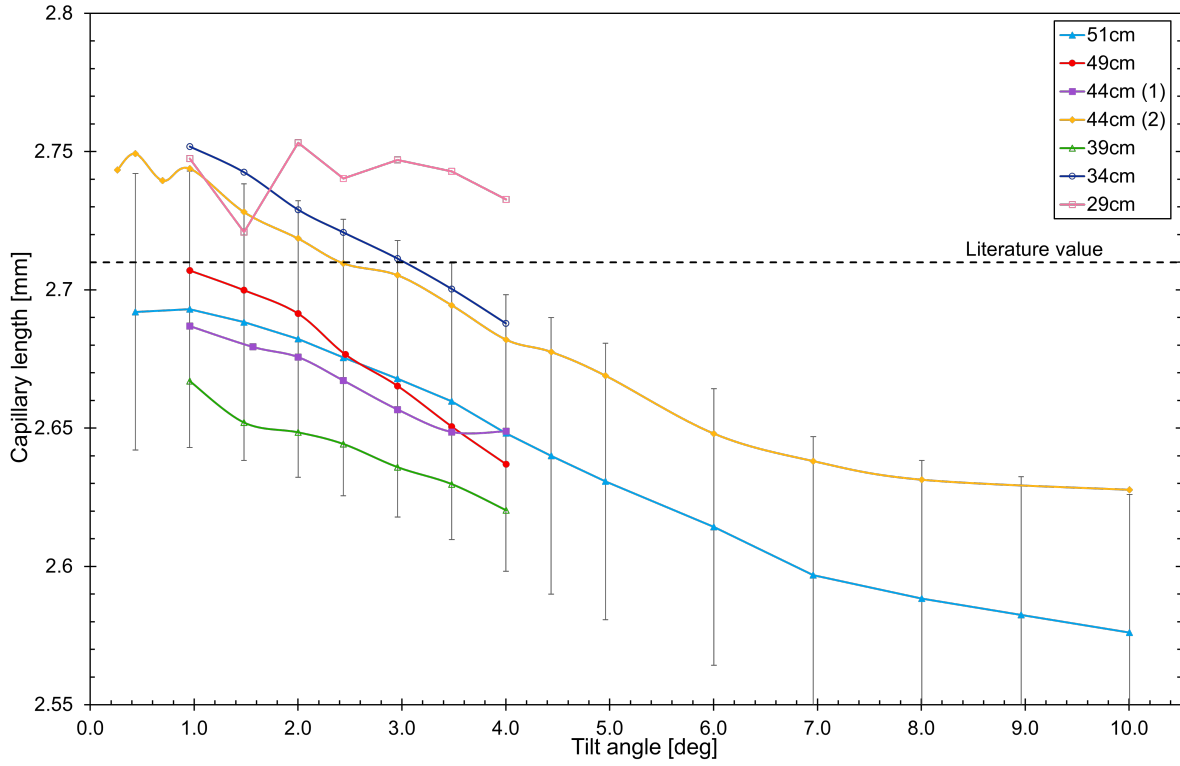


Figure S4: Plot of how the camera height changed the measured capillary lengths. The deviations shown are of the same order as those observed across many fillings of the trough and therefore there is no conclusive evidence to suggest the camera height causes any systematic error. Error bars have only been drawn on the 51 cm line for clarity. This is the only line that has been calculated by averaging over many fillings of the trough.

S.1.4 Camera distance

Some of the approximations made are dependent on the distance between the camera and checkerboard as discussed by Moisy et al.[14] who conclude the camera should be placed far away. The scale calibration (Section 3.2) leads to the opposite conclusion, as the camera distance changes the number of camera pixels that each checkerboard square occupies. Therefore, moving the camera closer increases the resolution in the region of interest. There are also more practical constraints including that increasing the camera distance increases the effect of vibrations. There therefore must be an optimum distance for the camera. To test this data for many different distances was collected. This data is shown in Fig.S4. For most distances, only one set of data was collected, with more time this would be improved upon. The line at 51 cm was collected over five fillings and is the data discussed in Section 4.2.

We observe that systematic differences are observed between each distance. These deviations are of the same order observed across different fillings as shown by the error bars on the 51 cm line. Considering the random nature of the systematic error for each line it is, therefore, most likely that these errors can be attributed to the fillings of the device rather than the camera distance. Even so, while testing it was noticed that smaller camera distances appeared to lead to more erratic behaviour as shown in the 29 cm line. It is for this reason, that the largest camera-screen distance was used for other experiments. Due to practical constraints, this was limited to 51 cm between LCD and camera lens.

S.1.5 Capillary length over time

An important consideration is how the measurements might change over time. Here the razor blade was tilted to 1° and photographs were taken every 2.5 min. Fig.S5 shows the results of one run. This was repeated several times yielding similar results. This shows an increase in the fitted capillary length over time. This is likely due to the evaporation/change in the fluid volume. The rate of change of the capillary length was observed to change between runs and was likely due to temperature changes. This plot indicates that experiments need to last less than 20 min to achieve the accuracy of <0.05 mm. This was consistently the case. With more time this would be an important area explore further to as many

experiments may need to take place over a longer time scale would need to be calibrated for this effect.

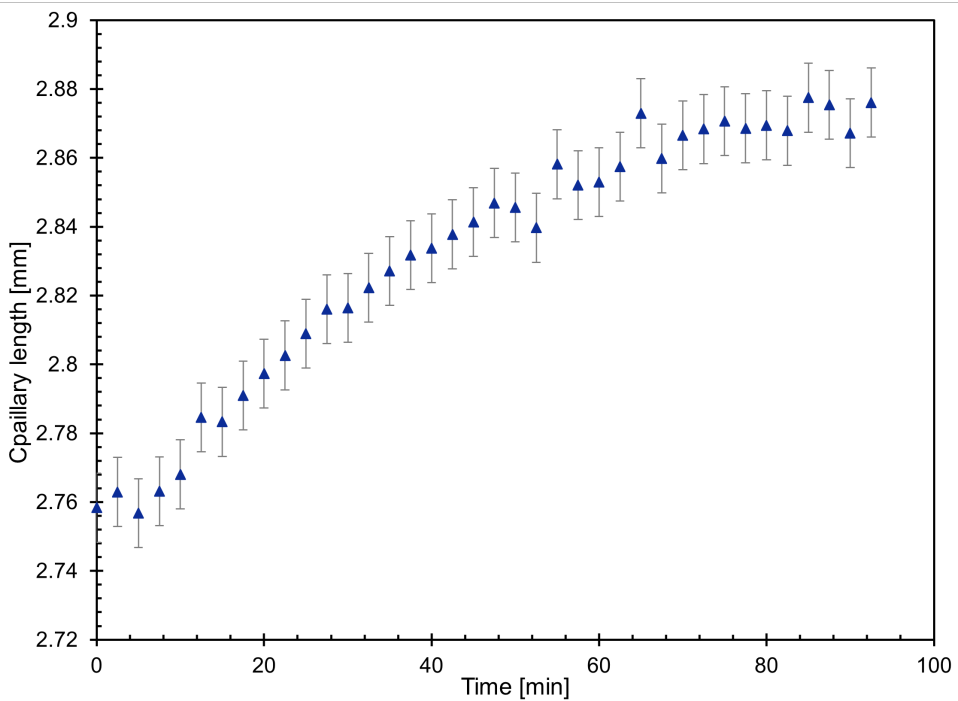


Figure S5: Plot of the fitted capillary length over time. Photos of the interface generated for a tilt angle of 1° were taken every 2.5min. Error bars of 0.003 mm have been drawn as the typical error observed between photographs. The plot shows a general increase in the measured capillary length. This indicates that experiments need to last less than 20 min to achieve the accuracy of <0.05 mm achieved in other aspects of the experiment.

S.1.6 Measuring a DPPC monolayer

DPPC² at an air/water interface forms a monolayer the properties of which have been extensively measured[36–39].

The DPPC in a 1 mg/mL solution of chloroform³ was added in increments of 1 μL to the water surface. The surface was then left for a few seconds before images were taken. Before any measurements were taken the trough was washed and filled before taking the reference image. The razor blade was tilted and a set of data was taken to record the capillary tension without a monolayer.

Fig.S6 shows the plot of four runs of data for two different tilt angles and two different fillings for these angles. Also plotted is the literature curve[36]. Primarily we observe the major horizontal shift between this data and the literature curve. This may be caused by the somewhat unknown DPPC concentration. To resolve this, data for the same DPPC sample, using a traditional Langmuir trough would have been taken, however, there was insufficient time in this project to complete this. Two runs per angle were taken, comparing these there is a clear offset between them likely the result of the filling volume effects discussed in Section 4.2. The other observed effect is that the curves for the two different angles are distinct. A possible explanation would be the effect observed in Section 4.2 where the angle changed the measured capillary length due to the first-order solution used and that a similar effect is observed here. To make the device more versatile it would therefore be necessary to explore this field further to ensure that the device is capable of replicating the results from other methodologies. To do this more results would need to be taken, specifically at more tilt angles and performing more runs per angle.

²1,2-dipalmitoyl-sn-glycerol-3-phosphocholine.

³Chloroform dissolves PLA so care was taken to minimise the possibility of this.

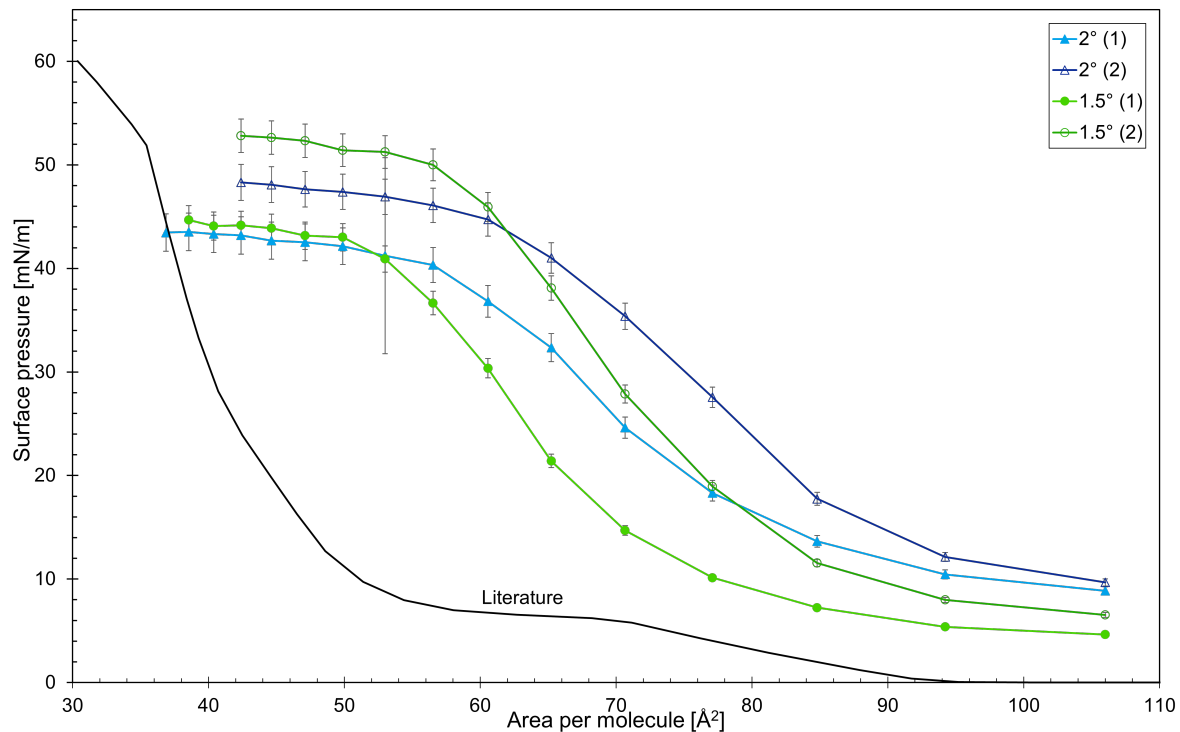


Figure S6: Plot of the surface pressure against the area per DPPC molecule for four runs of data. Also plotted is the literature curve for similar experiments[36]. This shows the general decrease in surface pressure with area per molecule as predicted by the literature. However, this does also show the distinct differences between the curves for each angle and the literature curve.

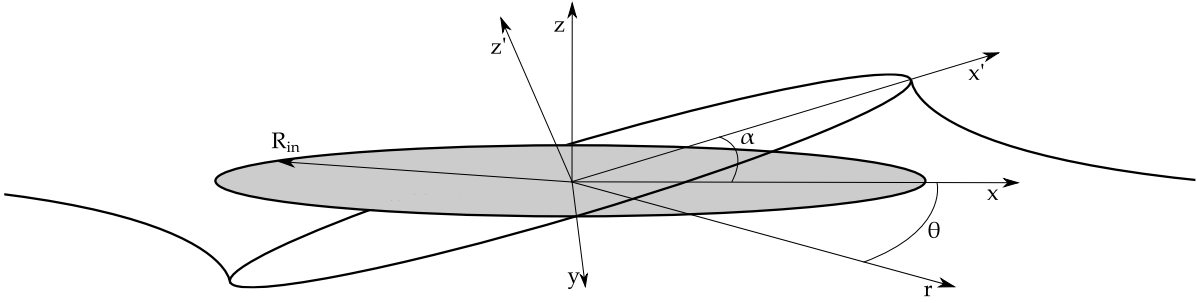


Figure S7: Diagram of the tilted disk showing the naming convention used.

S.2 Testing a circular tilting interface

Another choice of tilting interface would be like Moleai & Crocker, a disk. A solution for the Young-Laplace equation has been proposed by my collaborator Prof. Dominic Vella (Oxford). I, therefore, attempt to demonstrate if this solution provides an accurate description of the surface generated.

S.2.1 Theoretical perspective

I begin with a discussion, adapted from Vella's solution to a disk tilted at an angle. Vella's original solution was to first order only. Here I have expanded this to third-order. This was done so that comparisons could be made to test how the errors between these solutions and a numerical solution change when including these additional terms.

If the coordinate axes are aligned so x' and y' are co-planer to the disk and z' is along the axis of the disk. Then without loss of generality, we can assume a rotation of the disk is along the y' axis. This gives the standard transformation

$$\begin{pmatrix} x \\ y \\ z \end{pmatrix} = \begin{pmatrix} \cos(\alpha) & 0 & -\sin(\alpha) \\ 0 & 1 & 0 \\ \sin(\alpha) & 0 & \cos(\alpha) \end{pmatrix} \begin{pmatrix} x' \\ y' \\ z' \end{pmatrix}, \quad (\text{S1})$$

where the un-primed axes are relative to the surface of the undistorted fluid so that x is co-planar to the surface of the fluid. Therefore, the perimeter of the disk is given by

$$x'^2 + y'^2 = R_{in}^2. \quad (\text{S2})$$

Hence, in the un-primed coordinates, the edge of the disk is an ellipse given by the equation

$$\left(\frac{x}{\cos(\alpha)} \right)^2 + y^2 = R_{in}. \quad (\text{S3})$$

Using the cylindrical coordinate system where $x = r(\theta) \cos(\theta)$, $y = r(\theta) \sin(\theta)$, and $z = z$ the height of the edge of the disk given by

$$h = x \tan(\alpha) = r(\theta) \cos(\theta) \tan(\alpha). \quad (\text{S4})$$

After some rearranging, the edge of the disk is given by

$$r(\theta) = R_{in} [1 + \frac{1}{2} \tan^2(\alpha) (1 + \cos(2\theta))]^{-1/2}. \quad (\text{S5})$$

Assuming α is small and keeping terms only to third-order we arrive at

$$r(\theta) = R_{in} [1 - \frac{\alpha^2}{4} (1 + \cos(2\theta))], \quad (\text{S6})$$

and therefore

$$\frac{h}{R_{in}} = (\alpha - \frac{\alpha^3}{24}) \cos(\theta) - \frac{\alpha^3}{8} \cos(3\theta). \quad (\text{S7})$$

The fluid surface is determined by the Laplace–Young equation which, keeping only linear terms and writing $l_c = \sqrt{\frac{\gamma}{\rho g}}$ is

$$\nabla^2 z = \frac{z}{l_c^2}. \quad (\text{S8})$$

Using separation of variables and applying the boundary conditions where $h \rightarrow 0$ as $r \rightarrow \infty$ and $z = h$ on $r(\theta)$ in cylindrical coordinates this has the general series solution

$$z = \sum_{n=0}^{\infty} A_n K_n(r/l_c) \cos(n\theta), \quad (\text{S9})$$

where A_n are coefficients to be determined and $K_n(r/l_c)$ are the modified Bessel functions of the second kind of order n . On $r(\theta)$ we can expand the Bessel functions to terms in α^3 so the n^{th} term (for $n > 0$) becomes

$$A_n [K_n(R_{in}/l_c) \cos(n\theta) - \frac{R_{in}}{8l_c} \alpha^2 K'_n(R_{in}/l_c) (\cos((n-2)\theta) + 2\cos(\theta) + \cos((n+2)\theta))]. \quad (\text{S10})$$

From here on for simplicity we define $K_n = K_n(R_{in}/l_c)$ and likewise for the derivatives with respect to the argument. Using the equation for h can see that only terms for $n = 1, 3$ are required. The $n = 3$ term will have a $\cos(5\theta)$ which we will ignore but can be shown to be removed by considering higher order terms. Collecting terms in $\cos(\theta)$ and $\cos(3\theta)$ and coupling some of the constants into $Q = \frac{R_{in} K'_1}{8l_c K_1}$ and remembering that $\cos(-\theta) = \cos(\theta)$ gives:

$$\cos(\theta) : A_1 K_1 [1 - 3Q\alpha^2] - A_3 Q K'_3 \frac{K_1}{K'_1} \alpha^2, \quad (\text{S11})$$

and

$$\cos(3\theta) : -A_1 K_1 Q \alpha^2 + A_3 [K_3 - 2Q K'_3 \frac{K_1}{K'_1} \alpha^2]. \quad (\text{S12})$$

Written in matrix form

$$\begin{pmatrix} K_1 [1 - 3Q\alpha^2] & -Q K'_3 \frac{K_1}{K'_1} \alpha^2 \\ -K_1 Q \alpha^2 & K_3 - 2Q K'_3 \frac{K_1}{K'_1} \alpha^2 \end{pmatrix} \begin{pmatrix} A_1 \\ A_3 \end{pmatrix} = \begin{pmatrix} \alpha - \frac{\alpha^3}{24} \\ -\frac{\alpha^3}{8} \end{pmatrix}, \quad (\text{S13})$$

Inverting the matrix, computing the determinant to terms in α^3

$$\begin{pmatrix} A_1 \\ A_3 \end{pmatrix} = \frac{1}{K_1 K_3} \left[1 + \left[3Q\alpha^2 + \frac{2Q K'_3 K_1 \alpha^2}{K_3 K'_1} \right] \right] \begin{pmatrix} K_3 - 2Q K'_3 \frac{K_1}{K'_1} \alpha^2 & Q K'_3 \frac{K_1}{K'_1} \alpha^2 \\ K_1 Q \alpha^2 & K_1 [1 - 3Q\alpha^2] \end{pmatrix} \begin{pmatrix} \alpha - \frac{\alpha^3}{24} \\ -\frac{\alpha^3}{8} \end{pmatrix}. \quad (\text{S14})$$

Further expanding to third-order gives the expressions for A_1 and A_3 as

$$A_1 = \frac{\alpha}{K_1} + \frac{\alpha^3}{K_1} \left(3Q - \frac{1}{24} \right), \quad (\text{S15})$$

$$A_3 = \frac{\alpha^3}{K_3} \left(Q - \frac{1}{8} \right). \quad (\text{S16})$$

Therefore to first order, I recover Vella's solution namely

$$h(r, \theta) = \alpha R_{in} \frac{K_1(r/l_c)}{K_1(R_{in}/l_c)} \cos(\theta), \quad (\text{S17})$$

which is plotted in Fig.S8. The first and third-order solutions were compared to surfaces generated by Surface Evolver, however, this work could not be completed in time. There were however indications that the third-order solution did provide a better description of the surface. Both solutions appeared to show deviations that grew quadratically with α , suggesting that neither solution forms a complete description of the surface.

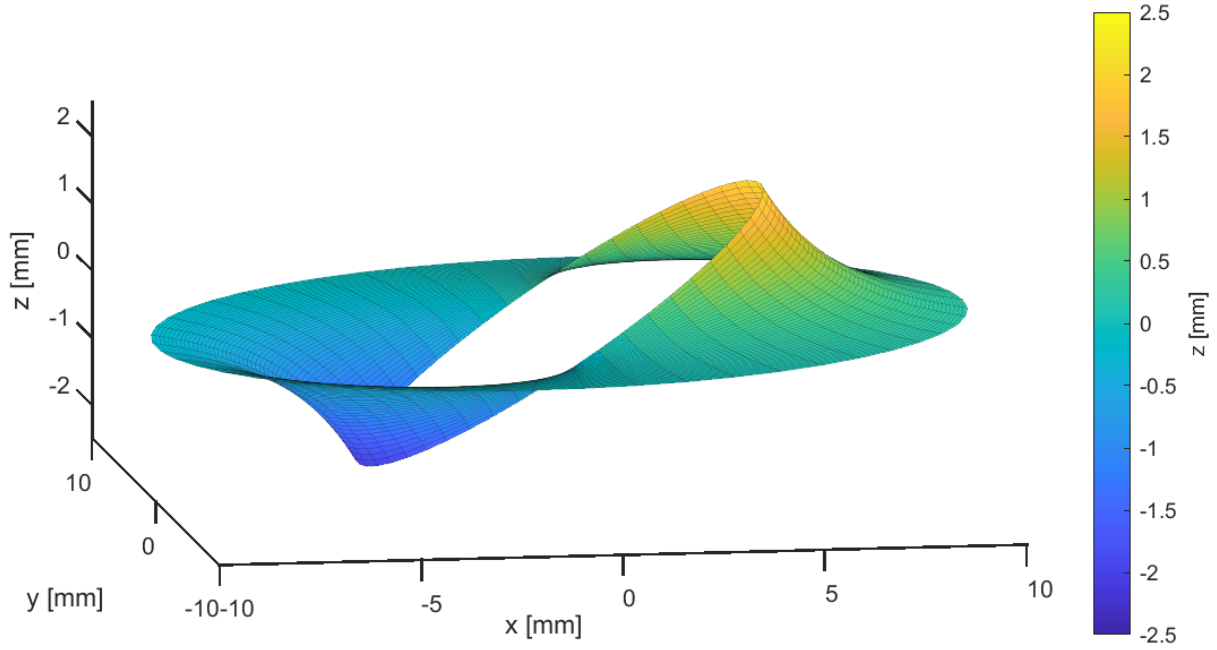


Figure S8: Plot of Vella's solution to the Young-Laplace equation for a tilting disk given by Eq.(S17). Plotted for $R_{in} = 5\text{mm}$ and $\alpha = 23^\circ$ and $l_c = 2.7\text{mm}$. The vertical range has been restricted to avoid plotting the discontinuity at the origin.

As a check of the first order solution we take the limit as the radius of the disk becomes infinitely large as one would predict Eq.(S17) to tend to the first order solution for a straight edge,

$$h = w \sin(\alpha) e^{-(x-w \cos(\alpha))/l_c}, \quad (\text{S18})$$

for a distance x from the pivot and w being the length of the edge from the pivot.

Taking the form of the modified Bessel functions from the DLMF[40].

$$K_n(r) = \left(\frac{\pi}{2r}\right)^{\frac{1}{2}} e^{-r} \left(\sum_{k=0}^{\ell-1} \frac{a_k(n)}{r^k} + R_\ell(n, r) \right). \quad (\text{S19})$$

Hence, in the limit where $w = R_{in}$ and $l_c \ll R_{in}$ and therefore $l_c \ll r$ because we are only interested in the region near the boundary. The Bessel function to leading order in r leaves

$$K_n\left(\frac{r}{l_c}\right) = \left(\frac{\pi l_c}{2r}\right)^{\frac{1}{2}} e^{-r/l_c}. \quad (\text{S20})$$

Therefore, Eq.(S17) simplifies to

$$\alpha R_{in} \sqrt{\frac{R_{in}}{r}} e^{-(r-R)/l_c} \quad (\text{S21})$$

Where the θ dependence has been removed in the limit of large R . We are only interested in the region near the boundary; so, for large R the ratio R/r converges to 1 and can be neglected. Hence this can be seen to converge on the solution for an infinite straight edge to first order in α as expected.

To fit this solution to the data it is necessary to write it in a Cartesian coordinate system because the camera pixels form a rectangular array. I also add the necessary rotational and translational transformations required for fitting to FCD data.

$$h(x, y) = A \cos(\omega_x) \cos(\omega_y) \cos(\theta) \frac{K_1\left(\frac{\sqrt{(x-t_x)^2+(y-t_y)^2}}{l_c}\right)}{K_1\left(\frac{R_{in}}{l_c}\right)} + \sin(\omega_y)x + \sin(\omega_x)y + t_z \quad (\text{S22})$$

where

$$\cos(\theta) = \frac{\cos(\omega_z)(x - t_x) + \sin(\omega_z)(y - t_y)}{\sqrt{(x - t_x)^2 + (y - t_y)^2}} \quad (\text{S23})$$

fitting parameters are discussed in Table S.21.

Parameter	Meaning
A	Vertical scaling
l_c	Capillary length
t_x	x translation
t_y	y translation
t_z	z translation
ω_x	x rotation
ω_y	y rotation
ω_z	z rotation
R_{in}	Radius of the disk

Table S.21: Fitting parameters used in Eqs.(S22) and (S23).

S.2.2 Method and results

To test the analytic solution for a circular interface, a disk with a diameter of approximately 5 cm with a sharp edge was manufactured by Dr Jurij Kotar. This disk is shown in Fig.S9.

Following a similar procedure to that of the straight edge, the theoretical curve was fitted to data taken for a disk interface. However, due to reduced symmetry compared to the straight edge, two additional translations must be considered. While testing, it was found that the x translation, t_x , was imperative to fix. Because the camera was initially aligned to the edge of the disk it was possible to set $t_x = R_{in}$. Results of this are shown in Fig.S10. Having done this it was found that Vella's solutions fits well for small angles, Fig.S10a, with errors between the measured surface and Vella's solution being less than 2% of the maximum height, normalising in this way allows comparison of errors between the plots. However, for larger angles, the fit quickly becomes poor with errors over 20% of the maximum height.

Critically Vella's solution does not appear to have the same angular dependence that is observed in the data collected. This may be due to the FCD. To test this a different region of the curve would be imaged. For example at 45°. This would test if the discrepancy is due to the imaging method or a real difference from the analytic solution. This could also be tested by comparing these plots to numerical surfaces generated by Surface Evolver. This was attempted but could not be completed adequately in the time permitted.

It is worth considering that the radius of the disk is more than twice the razor blade width therefore the approximations would be expected to break down for smaller angles. That said as shown in Section 4.1 the first-order solution for a straight edge modelled the solution well up to at least 2 mm of lift whereas Vella's solution appears to break down before 1 mm of lift.

However, overall Vella's solution does appear to show reasonable agreement with the measured plots but further work would be required to provide a fuller discussion of the accuracy and the working range of the solution.

An interesting alternative would be to instead of tilting the disk to raise the disk above the fluid surface. This would reduce the number of approximations required in the derivation and would be less sensitive to inaccuracies in the location of the tilt axis.

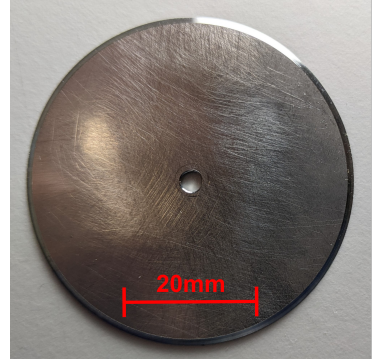


Figure S9: Photo of the disk used to measure the surface generated by a tilted disk. This shows the central mounting hole and the sharp edge.

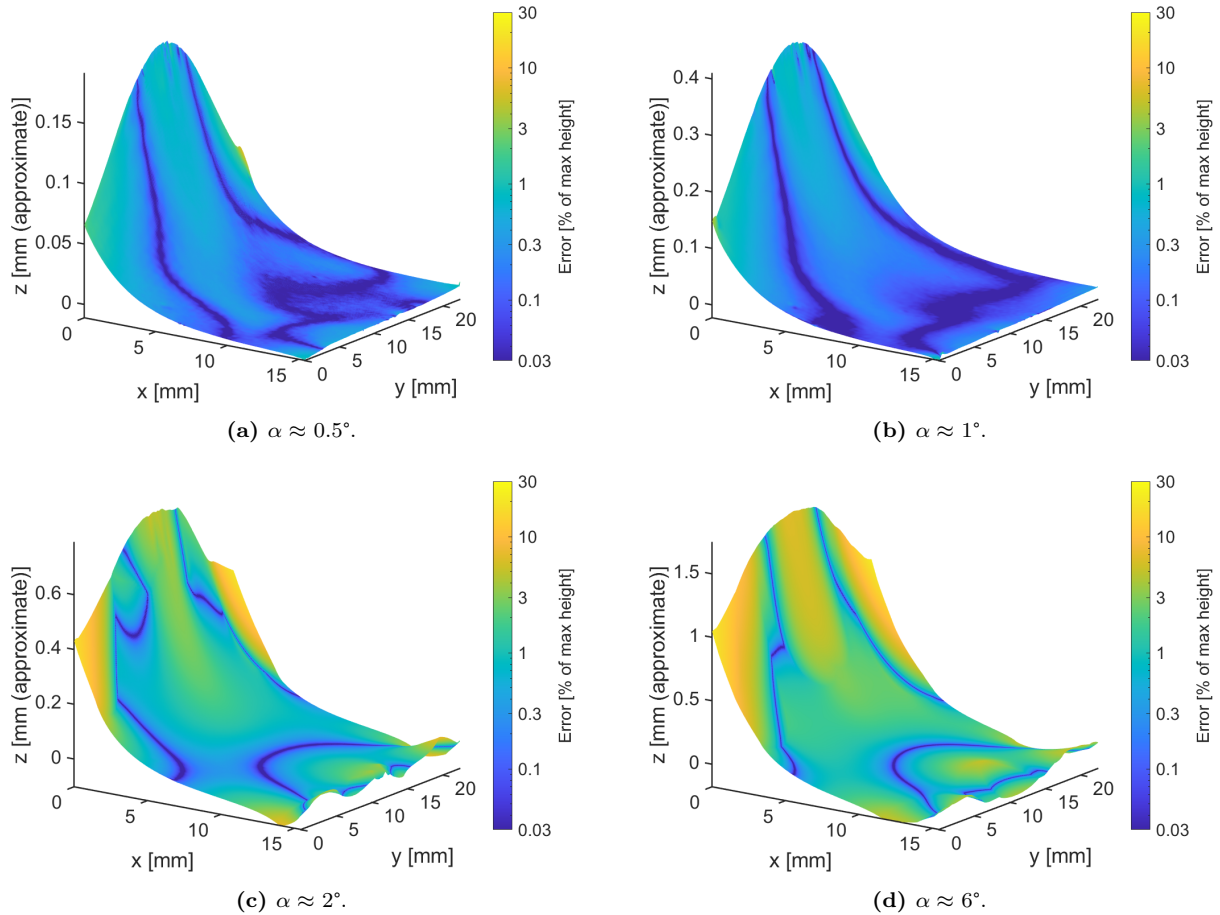


Figure S10: Plots of the surface generated by a tilting disk for different tilt angles. Plots are taken in the region near $\theta = 0^\circ$ and are coloured with the error compared to Vella's solution. These show the increase in error with tilt angle as well as the poor angular fit between the reconstructed surface and Vella's solution. The vertical scale has been approximated using the same method as in Section 4.1.